Universidad de La Laguna
Instituto de Astrofísica de Canarias

Trabajo de Fin de Máster

UNIDENTIFIED FERMI SOURCE (UFO) IN AN ACTIVE GALACTIC REGION

Author

Jorge Otero Santos

Supervised by

Alicia López Oramas
&
Ramón García López

La Laguna, June 3, 2018

Facultad de Ciencias
Universidad de La Laguna - Departamento de Astrofísica

Resumen (Abstract)

La aparición de los telescopios Cherenkov y la técnica por imagen Cherenkov (IACT por sus siglas en inglés) en la década de los 70 han supuesto un gran avance en la astronomía de rayos γ. Dado que la atmósfera es opaca a radiaciones tan energéticas como los rayos X o los rayos γ, técnicas de detección indirecta fueron desarrolladas para permitir la detección de objetos en este rango de energías desde la Tierra. Estos telescopios son capaces de detectar las cascadas de partículas que generan los rayos cósmicos y los rayos γ cuando entran en la atmósfera e interactúan con las partículas presentes en ella. El resultado de estas interacciones es un haz de luz de muy corta duración, conocido como luz Cherenkov, producido debido al paso de partículas cargadas que viajan por el medio (la atmósfera) a una velocidad superior a la velocidad de la luz en dicho medio. Actualmente ésta es una de las líneas de estudio más prometedoras, y que nos permite estudiar los objetos más violentos del Universo y los procesos físicos que tienen lugar en ellos.

Gracias a la última generación de telescopios Cherenkov como MAGIC, H.E.S.S. o VERITAS, y a satélites como *Fermi*-LAT, que opera en altas energías, varios cientos de fuentes han sido detectadas en la actualidad, como remanentes de supernovas, núcleos activos de galaxias o sistemas binarios. Muchas de ellas sin embargo todavía se encuentran sin identificar o sin una clara asociación a otra fuente conocida. Recientemente se han detectado rayos γ provenientes de una región de formación estelar conocida como "Cygnus Cocoon", siendo la primera de su naturaleza en detectarse en este rango del espectro. Además, varias fuentes candidatas a ser otras regiones de formación estelar han sido detectadas también en energías de GeV y TeV, como Westerlund 1 y 2 o 30 Doradus. Estas regiones se caracterizan por la presencia de una estrella masiva OB (o una asociación de estrellas OB), con fuertes vientos estelares capaces de acelerar las partículas presentes en ellos y, consecuentemente, producir rayos γ. Además, se observa en estas regiones una estructura en forma de burbuja debido a la estrella OB. Estas estructuras de burbuja son similares a la observadas en regiones HII, con grandes cantidades de emisión infrarroja a una longitud de onda de 8 μm.

En este proyecto estudiaremos una de estas posibles regiones de formación estelar, previamente detectada con el satélite *Fermi*-LAT, y observada por los telescopios MAGIC durante el año 2017. Esta fuente, conocida como 2FHL J1839.5-0705, incluida en el catálogo 2FHL de *Fermi*-LAT, se encuentra en una región muy poblada de fuentes emisoras en muy altas energías.

El objetivo principal de este trabajo será por lo tanto confirmar la detección de esta fuente en el rango de energía en el que operan los telescopios MAGIC, y caracterizar y analizar dicho objeto, distinguiéndolo del resto de fuentes en los alrededores. Se tratará de ajustar la posición y extensión de la fuente, contrastando los resultados obtenidos con la bibliografía existente. Además, se extraerán el espectro y la curva de luz de 2FHL J1839.5-0705 y se derivarán algunas características que permitirán comparar esta fuente con las demás regiones de formación estelar (o posibles regiones de formación estelar), buscando información que ayude a confirmar la naturaleza del objeto. Finalmente se tratarán de estudiar en menor detalle algunas de las fuentes más brillantes de la región en la que se encuentra.

El esquema del proyecto es el que se detalla a continuación:

- En la Sección 1 se introduce la astronomía de rayos γ y de muy altas energías, incluyendo un breve resumen de esta línea de investigación a lo largo del siglo XX, resaltando los hechos principales que han desencadenado su gran evolución hasta llegar a las técnicas utilizadas en la actualidad. Se detallan además las motivaciones que han llevado a la realización de este trabajo, además de los objetivos principales que se esperan alcanzar con este estudio.

- La Sección 2 contiene los fundamentos teóricos y conceptos necesarios para la realización del análisis y la correcta comprensión de los resultados obtenidos. Se detallarán las características de los rayos cósmicos y los rayos γ. Se describen algunos de los principales objetos en los que se generan y los procesos físicos involucrados. Por último, se exponen las bases de la técnica de detección por imagen Cherenkov y las consideraciones a tener en cuenta a la hora de detectar una cascada generada por un rayo γ o un rayo cósmico y discernir entre ambas.

- La Sección 3 comienza con una breve descripción de los aspectos fundamentales de los telescopios MAGIC y sus características principales (mecánica, electrónica, sensibilidad...). A continuación se detalla la cadena de análisis necesaria para la reducción de datos tomados con estos telescopios, dando especial importancia al software utilizado y a las rutinas necesarias para la realización de este estudio.

- Los resultados del análisis realizado están expuestos en la Sección 4. Se comienza con una breve descripción de la región en la que se encuentra la fuente estudiada, caracterizando también las fuentes presentes en sus alrededores. A continuación se expone información sobre las observaciones realizadas con los telescopios MAGIC y de los datos con los que se va a realizar el análisis. Finalmente se detallan los resultados del mismo, a la vez que se discuten las posibles implicaciones de estos resultados. Además, se hará una breve exposición de los posibles mecanismos de aceleración de partículas hasta energías del orden de TeV que pueden tener lugar en una región de formación estelar.

- En la Sección 5 se exponen las conclusiones extraídas de este análisis y de los estudios realizados.

- Finalmente en la Sección 6 se recogen algunas perspectivas futuras, tanto generales con respecto a la astronomía de rayos γ y muy altas energías, como enfocadas a profundizar más en el estudio de esta fuente y de otras regiones de formación estelar.

- El proyecto cuenta también con un apéndice gráfico donde se incluyen las figuras de menor relevancia en el análisis, y un apéndice bibliográfico donde se encuentran enumerados todos los artículos, libros y recursos consultados para la realización de este trabajo.

Contents

1. Summary

Very high energy (VHE) astronomy concerns the study of sources of γ-ray photons, with energies above 100 GeV, up to several TeV, being one of the most recent windows in the electromagnetic spectrum opened to be studied. Back in the 50's, Cherenkov radiation asociated with extragalactic high energy sources was detected, and since then, several telescopes were built for this purpose.

This field has experimented an enormous growth since the 50's, closely related to the study of cosmic rays and cosmic-ray air showers. The first detection of Cherenkov radiation due to this cosmic-ray showers back in 1953 by Galbraith & Jelley [1] opened a new possibility of using this phenomenon to study high energy sources, what led to the development of techniques and facilities dedicated to this field in the 60's. It was not however until the appearance of the imaging technique when the high energy astronomy really became as important as it is today. The last four decades have been the golden age of the VHE and the γ-ray astronomy, with the construction of ground-based and space-based observatories.

Ground-based observatories started to raise in importance with the development of the imaging technique, resulting in the Imaging Atmospheric Cherenkov Telescopes (IACTs). Since 1989, several IACTs were built around the world. During this period of time, the most important projects in this field were Whipple, a 10 m diameter telescope placed at Mt. Hopkins, Arizona, which made the first VHE observation of the Crab Nebula back in 1989 [2], CAT (Cherenkov Array at Themis), located in the French Pyrenees, and HEGRA (High Energy Gamma Ray Astronomy), on the Canary island of La Palma, at the Roque de los Muchachos Observatory, leaders of the VHE astronomy. Now, the third generation of IACTs is operating, headed by three projects: H.E.S.S. (High Energy Stereoscopic System), located in the Khomas Highland in Namibia, MAGIC (Major Atmospheric Gamma-ray Imaging Cherenkov Telescope), located at the Roque de los Muchachos Observatory, and VERITAS (Very Energetic Radiation Imaging Telescope Array System), at the Fred Lawrence Whipple Observatory in southern Arizona. The next generation is under construction right now with the Cherenkov Telescope Array (CTA), an observatory that will improve the sensitivity of current IACTs in at least four orders of magnitude in energy, with improved angular and energy resolution [3][4].

At the same time, a different type of ground-based telescopes were developed, based on Water Cherenkov Detectors to detect γ-rays at several TeV and/or cosmic rays. The MILAGRO experiment was one of the first generations of this detectors, followed by other observatories like the Tibet Air-Shower Array and ARGO-YBJ at the YangBaJing Cosmic Ray Observatory. The last ones of this type of instruments are HAWC (High Altitude Water Cherenkov) in Mexico and the Pierre Auger Observatory in Argentina, currently working [5].

With the rising importance of γ-ray astronomy, space-based observatories also began to be launched, with instruments that allowed to make direct observations of high-energy sources. Some of the most important missions are SAS-2 (Small Astronomy Satellite 2), EGRET (Energetic Gamma Ray Experiment Telescope) [6] or AGILE (*Astrorivelatore Gamma ad Imagini Leggero*) and its main instrument, GRID (Gamma Ray Imaging Detector). Since 2008, the instrument *Fermi*-LAT (Large Area Telescope) at *Fermi* γ-ray Space Telescope is operative, observing γ-rays with energies between 20 MeV and 300 GeV [4][7].

1.1. Motivation and objectives

In this project we will focus on VHE γ-rays and the imaging technique. Specifically, we will make use of the MAGIC telescopes, as we are going to analyze a VHE source detected by *Fermi*-LAT named 2FHL J1839.5-0705, using data taken in 2017 during three different periods (June, July and August 2017). 2FHL J1839.5-0705, which was detected by *Fermi*-LAT up to 500 GeV and included in the Second *Fermi*-LAT Catalog of High Energy Sources (2FHL) [8], is located in a populated region where other VHE sources are detected. Observations of the different structures emitting infrared and radio near our high energy source indicate that it may be a star-forming region (SFR).

The goal of this project, thus, is to characterize and analyze 2FHLJ1839.5-0705 in VHE and distinguish it from the rest of the sources in the surroundings already detected by *Fermi*-LAT. To achieve this objective we will make use of MARS software (Magic Standard Analysis Software), written in C++ and mainly used for the analysis of MAGIC data. In case of detecting the source and if its SFR nature is confirmed, it will be one of the first star-forming regions ever detected at VHE, opening new possibilities for future and further studies. In the following sections we will describe the basics of γ-ray astronomy and the MAGIC telescopes, as well as the tools needed to perform the data analysis. We will finally present the results of this project and discuss the achieved goals and future prospects.

2. Introduction: Cosmic Rays and γ-Ray Astronomy

2.1. Cosmic Rays

Cosmic rays (CRs) are an ionising radiation discovered by Victor Hess in 1912 thanks to a balloon flight at 5300 meters of altitude. This radiation is composed by subatomic particles, mainly protons ($\sim$89%), but also α particles (helium nuclei, $\sim$9%), electrons and positrons ($\sim$1%), heavier nuclei such as carbon (C), oxygen (O) or nitrogen (N) ($\sim$1%) and neutrons, neutrinos (ν) and γ-rays ($\sim$0.1%). CRs reach Earth from both galactic and extragalactic sources.

The CR energy spectrum spans over 13 orders of magnitude, from 10^9 to 10^{21} eV (see Figure 1). It can be approximated by a series of power laws ($F \sim E^{\alpha}$) associated to non-thermal processes. At low energies, the spectrum is described by a power law with index $\alpha = -2.7$, changing to $\alpha = -3.3$ at 10^{15} eV (1 PeV). This softening of the spectrum creates the first feature, the *knee*. At 10^{18} eV (1EeV), the spectrum can be adjusted to a power law with index $\alpha = -2.7$, where the second feature, known as the *ankle*, is located [9].

Low energy CRs are very common and they are modulated by the solar flux. Particles with energies below the *knee* come from galactic sources with a frequency of 1 particle/cm^2 $\cdot$ year, while the most energetic particles, above the *ankle*, are thought to come from extragalactic objects [10]. The origin of the CRs with energies located between the *knee* and the *ankle* is still under discussion, but an important source of galactic cosmic rays up to PeV energies seems to be the Galactic Center [11].

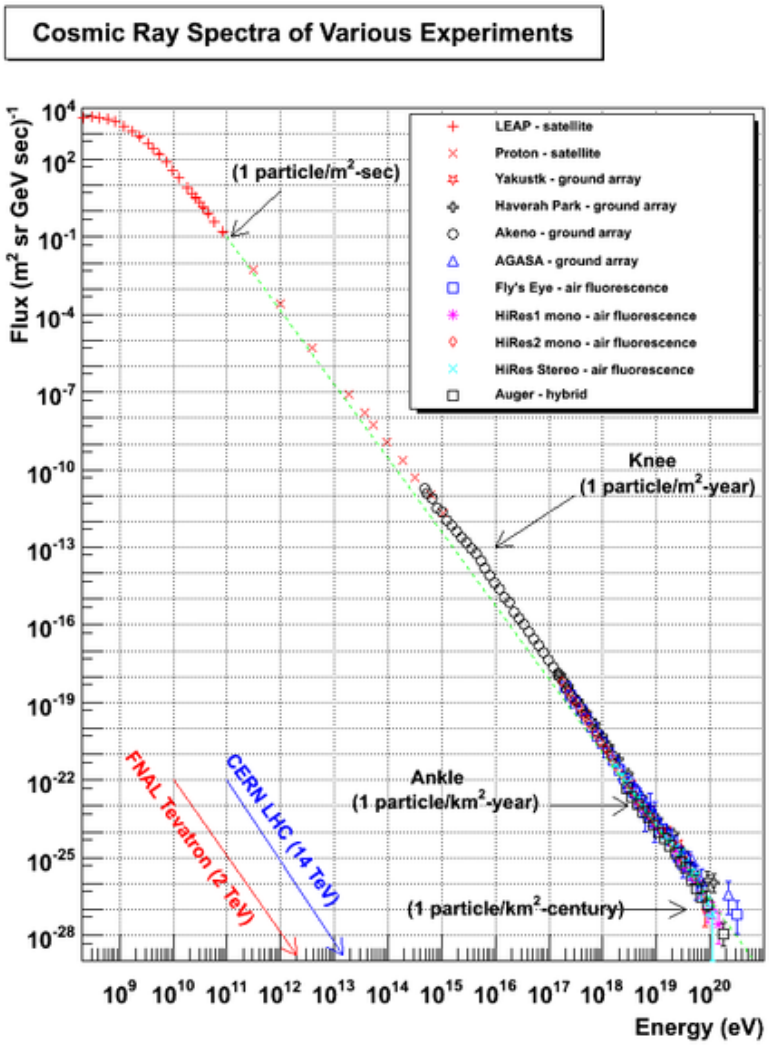

Figure 1: Cosmic ray spectrum measured by several experiments. The dotted line represents an E^{-3} power law for comparison. The energies reached by current experiments are represented by the red and blue arrows. *Source: http://www.physics.utah.edu/∼whanlon/spectrum.html.*

2.2. Very High Energy γ-Ray Astronomy

CRs are charged particles, and as such, they are deflected by galactic, extragalactic and Earth's magnetic fields, which implies that is not a simple task to constrain the incoming direction. One way to know the posible origin is through the study of γ-rays produced by charged particles via different non-thermal mechanisms.

γ-ray refers to those photons with an energy above 100 keV (10^5 eV), up to energies greater than 10^{20} eV, expanding more than 15 decades in the electromagnetic spectrum. Due to the wide energy range involved, a classification has been made in order to stablish more precisely in which order of magnitude are we working.

We can classify as low/medium energy (LE/ME) γ-ray astronomy the energy range between 0.1 and 30 MeV, high energy (HE) γ-ray astronomy from 30 MeV to 100 GeV, very high energy (VHE) γ-ray astronomy to those photons with an energy between 100 GeV and 100

TeV and ultra high energy (UHE) γ-ray astronomy above 100 TeV. Several detection techniques have been developed, but for VHE and UHE astronomy, due to the low flux, big collection areas are required, which does not allow an efficient space-based detection. Henceforth we are going to focus on VHE astronomy, since in this project we will analyze data taken with the MAGIC telescopes, sensitive to energies between 50 GeV and 30 TeV. A thoroughful description of this telescopes is provided in Section 3.

Only a few hundreds of γ-ray sources are known so far. Some of the sources we can detect at this energies are for example[1]:

- Active Galactic Nuclei (AGNs): AGNs are galaxies which host a supermassive black hole in their center, accreting matter from the surroundings. This causes the appearance of relativistic jets perpendicular to the galactic plane with perfect conditions for the acceleration of particles and the emission of γ-rays.

- Gamma-ray Bursts (GRBs): GRBs are one of the most violent and energetic events in the Universe, with a very short and intense γ-ray emission, able to outshine any other γ-ray source in the sky. According to the duration of the GRB, they are classified in short-duration and long-duration. The origin of this phenomenon is not yet clear, although it has recently been confirmed that binary neutron star mergers are the progenitors of short GRBs [14].

- Compact binaries: Systems composed by an OB/Be star and a compact object such as a neutron star or a black hole. γ-ray emission can happen via two different mechanisms: due to the interaction between the relativistic wind from a rotation pulsar with the stellar wind of the massive companion star, and also because of the accretion of matter by the compact object, creating an accretion disk and a relativistic jet [15].

- Pulsars and Pulsar Wind Nebulae (PWN): Pulsars are rapidly rotating neutron stars with a strong magnetic field, created from the remaining core of a massive star after its death. The rotation and the magnetic field generate an electric field able to accelerate charged particles, causing jets and γ-ray emission.

- Supernova Remnants (SNRs): After the death of a massive star in an explosion known as supernova, a large amount of the material is expelled into the surroundings, resulting in a compact object and a gas nebula formed by the ejected material, called supernova remnant. Charged particles can be accelerated in this objects, reaching enormous energies and making SNRs one of the main sources of cosmic rays in the Universe.

- Star-forming Regions (SFRs): These regions are dense concentrations of interstellar gas as molecular clouds, containing basically molecular hydrogen (H_2) and helium (He), with temperatures of 10-20 K. Star formation begins with the collapse of the denser parts of the cloud, which results in its fragmentation into clumps that will give place to protostars. Up to now, only a few star-forming regions have been detected at γ-ray energies such as the Cygnus Cocoon [16], Westerlund 1 [17] and 2 [18][19][20] or 30 Doradus [21].

[1] These are a few examples of what the VHE γ-ray astronomy can achieve. More detailed information at references [12] and [13].

The study of these objects can help the understanding of the different processes that generate VHE γ-ray photons and the physics involved. It is known that the most important mechanisms of production of γ-rays in astrophysics are[2]:

- Inverse Compton Scattering (IC): Collision of a high energy electron with a low energy photon, which is scattered up, creating VHE γ-rays. The scattering can be characterized by the equations of conservation of energy and momentum. Assuming a power law spectrum of the relativistic electrons with index Γ_e, the differential spectrum of the photons will be proportional to $E_\gamma^{-(\Gamma_e+1)/2}$. An ambient with a radiation field (star, cosmic microwave background) and an environment transparent to γ-rays is needed.

- Electron Bremsstrahlung: This phenomenon occurs when an incident charged particle (electron) is decelerated and deflected in an electric field, emitting radiation whose amplitude is proportional to the acceleration caused. In the astrophysical case, the resulting photons have energies of the same order as the incident electrons. These electrons can be characterized by a power law of index Γ_e, so the resulting γ-ray spectrum can also be approximated by a power law of index $\Gamma_\gamma \approx \Gamma_e$.

- Synchrotron radiation: It is created by relativistic electrons moving in a magnetic field. They describe a helical trajectory, emitting electromagnetic radiation beamed into a cone of angle $\theta \approx m_e c^2/E$. It showd a continuum spectrum with its maximum at a frequency ω_c, the critical frequency at which the maximum power is emitted, given by Equation (1),

$$\omega_c = \frac{3}{2}\frac{eH}{m_e c}\gamma^2 \sin\phi \tag{1}$$

  where ϕ is the angle between the direction of the magnetic field and the direction of the electron, e and m are the charge and the mass of the electron respectively, c is the speed of light, H is the intensity of the field and γ is the Lorentz factor, defined by $\gamma = (1 - v^2/c^2)^{-1/2}$, being v the velocity of the relativistic electron. Strong magnetic fields are required. Also, synchrotron radiation may act as a source of seed photons for IC scattering.

- Pion production and decay: Cosmic ray protons are very likely interacting with stationary hydrogen atoms and nuclei, producing excited states that give as a final product pions. This interaction has the following form:

$$p + p \longrightarrow N + N + n_1(\pi^+ + \pi^-) + n_2(\pi^0)$$

  where N is a proton or neutron and n_1 and n_2 are integers. The neutral pion π^0 has a very short lifetime ($\sim 10^{-16}$ s) and it can decay into two γ-rays with an energy of $\sim$70 MeV each.

$$\pi^0 \longrightarrow \gamma + \gamma$$

  The decay of excited states of the proton into hyperons and K mesons should also be taken into account, but since these processes are infrequent, they can generally be ignored.

[2]Each mechanism is more deeply explain at reference [13] and in the appendix of reference [22].

2.3. The IACT Technique

γ-rays can only be directly detected using space based detectors such as *Fermi* or AGILE [7], since the Earth's atmosphere is not transparent to this emission. However, they can indirectly be detected with ground observatories because of their interaction with the atmosphere, which starts at 15-35 km height and produces air showers. The product of these interactions are secondary particles and photons.

The resulting air showers can be classified mainly in two types: electromagnetic showers, product of the interaction of a γ-ray photon with a particle in the upper atmosphere, and hadronic showers, in which the primary interacting particle is a proton or a heavy nuclei. The Imaging Atmospheric Cherenkov Telescopes (IACTs) perform observations of the products of these showers by analyzing the images of the cascades, distinguishing between air showers of each type. This distinction between both types is made to eliminate the background introduced by hadronic cascades from the signal of the γ-ray source.

Hence, depending on the nature of the primary particle, three types of cascades are possible, if we also consider those produced by electrons (see Figure 2):

- Electromagnetic shower: It is originated by an incident VHE γ-ray photon. Because of its interaction with the Coulomb field of the atmospheric nuclei, a pair e^-- e^+ is created (via par production), and the energy of the photon is shared by these two particles. This pair can interact with the electromagnetic field of the nuclei in the atmosphere via Bremsstrahlung, emitting lower energy photons. If those photons have an energy higher than 1.022 MeV, they can create a new pair e^-- e^+. The repetition of this process gives place to the electromagnetic shower [23]. A simple way to describe the electromagnetic showers is using the Heitler model [24], which predicts accurately the most important features of this process. This model predicts that, after n interactions, there will be a total of 2^n particles in the shower, and the multiplication stops when de energy of the individual $e^{\pm}$ falls below a critical value ξ_c^e (85 MeV in air). This happens when the radiative energy loss of the secondary particles due to ionization is larger than their loss by Bremsstrahlung.

- Hadronic shower: In this case, the primary particle is a proton or nucleus interacting with the atmosphere. Different types of particles are created in this process, like muons, pions or kaons. Neutral pions (π^0) can decay into two photons, giving place to electromagnetic subshowers. These showers can be modeled similarly, generation keeps taking place until the energy of individual pions falls below a critical energy ξ_c^π. The main difference between electromagnetic and hadronic showers is that hadronic ones spread more so they are broader than the electromagnetics, and they produce a larger amount of different particles. Since these cascades are a very important contribution to the background, it is important to distinguish between them.

- e^- shower: The incident particle is an electron, and the result is similar to an electromagnetic cascade, as the products are only photons, e^- and e^+. These showers are an important contribution to the background and are very difficult to distinguish from the electromagnetic showers.

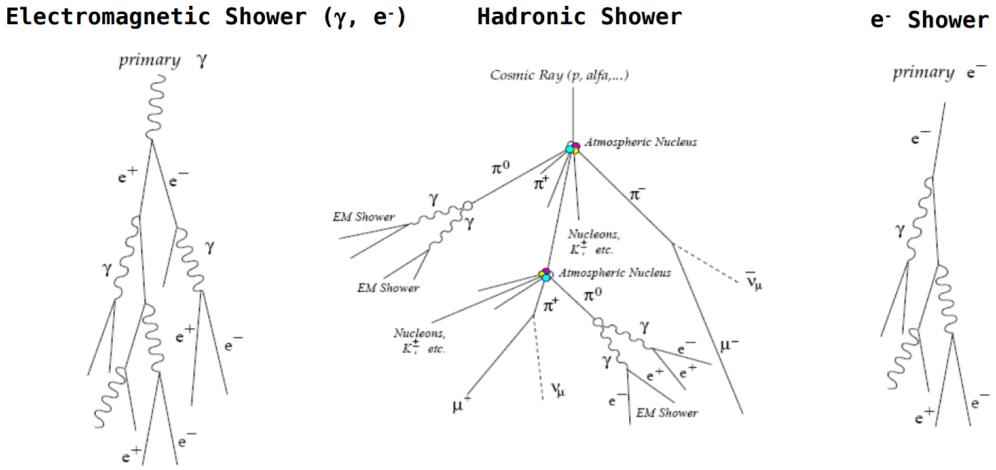

Figure 2: *Left*: Example of an electromagnetic air shower produced by an incident γ-ray, in which e^-, e^+ and photons are produced as secondary particles. *Center*: Example of a hadronic air shower, with several secondary particles such as pions (π^+, π^0, π^-), muons (μ^+, μ^-), kaons ($K^\pm$), photons or neutrinos (ν_μ, $\bar{\nu_\mu}$). *Right*: Example of an e^- shower produced by a primary e^-, where photons, e^- and e^+ are produced as secondary particles.

IACTs do not detect directly the incoming γ-rays, but the Cherenkov light [25] emitted by the products of the electromagnetic showers. The Cherenkov effect, discovered by Pavel Cherenkov in 1934, occurs when charged particles travelling in a dielectric medium with a refractive index n move with a velocity higher than the speed of light in that medium, defined by $c_{medium} = c/n$ [22]. When a charged particle moves in a dielectric medium, it disrupts the local electromagnetic field and polarizes this medium. If the particle is slow moving, this disturbance is symmetrical around and along the trajectory of the particle, and there won't be a residual electric field and therefore, neither will be any detectable radiation. On the other hand, if the particle is moving with $v > c_{medium}$, it polarizes this medium inducing a temporary dipole state. When the medium returns to the original state, the emission of a photon happens, originating a coherent wavefront moving with velocity v and an angle θ that depends on the refractive index, given by Equation (2).

$$\cos\theta = \frac{1}{\beta n} \tag{2}$$

The particle is moving ultra-relativistically, hence $\beta \sim 1$, and since Earth's atmosphere refraction index is $n_{atm} = 1.00029$, we obtain an emitting angle of $\theta = 1.3^o$. The resulting radiation propagates with a wavelength of approximately 350 nm at 2000 m, i.e. in the UV region of the electromagnetic spectrum. At this same height, the surface hit by the Cherenkov light has a radius of about 150 m.

Since IACTs do not detect directly the γ-rays emitted from the source but the Cherenkov radiation, we must distinguish between electromagnetic and hadronic showers. This differenciation is very importat due to the high background that hadronic showers introduce in the observations (the ratio γ-ray/charged cosmic ray is $\sim 10^{-4}$). The most efficient technique in the energy range of 100 GeV to 100 TeV, and used worldwide in all the operative Cherenkov telescopes, is the IACT technique. Depending on the number of telescopes involved, this tech-

nique can be performed with a monoscopic (one telescope) or a stereoscopic approach (at least two telescopes). The case in which we found ourselves is the stereoscopic imaging, based on the simultaneous detection of air showers with two or more telescopes separated a distance comparable to the Cherenkov light radius. Stereoscopic observations allow to reconstruct without ambiguity the parameters that describe the shower, to make a better γ/hadron separation and to reduce more effectively the background. The only inconvenient of the stereo imaging is the loss of detection rate caused by the overlap of the shower collection areas of individual telescopes [26].

In order to implement successfully this technique, IACTs need big collection areas due to the very low flux of VHE sources, and a fast camera with a high gain, sensitivity and efficiency. This is achieved with a camera composed of photomultiplier tubes (PMTs) [27]. Big collection areas and high efficiency also contribute to lower the energy threshold, since $E_{th} \propto 1/A \cdot \epsilon$. Additionally, data acquisition systems able to handle very high rates are needed.

The mirror surface reflects the Cherenkov light into the camera. To make the distinction between electromagnetic and hadronic showers, the image formed in the pixelized camera is analyzed, and depending on the shape and geometry of the image, γ/hadron separation can be performed. While electromagnetic cascades form a compact ellipse in the camera, hadronic showers have a more irregular, chaotic and broader shape [26]. An example of this can be seen more clearly in Figure 3.

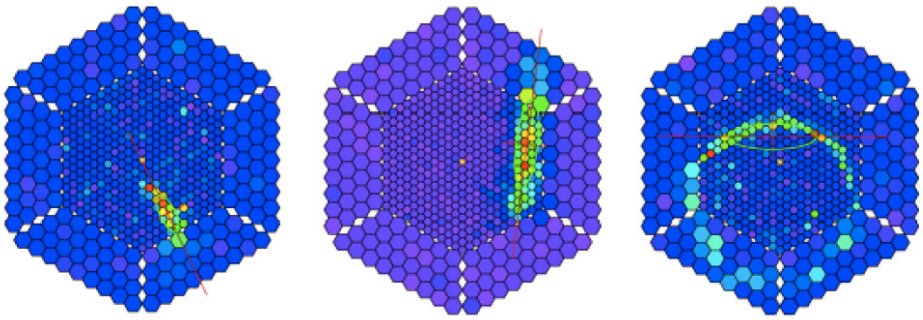

Figure 3: *Left*: Example of an image of an electromagnetic shower, with a compact and elliptical shape. *Center*: Example of an image formed by a hadronic shower, broader than the γ-ray cascade. *Right*: Characteristic ring shape image of a muon detection. *Credit: MAGIC Collaboration.*

To reconstruct the direction and energy of the primary γ-ray and discriminate it from hadronic showers, the IACT technique is based on a series of parameters called de Hillas parameters [28] that contain all the properties of the image, modelled as an ellipse. These parameters include (see Figure 4):

- *Size*: Total charge collected in terms of the number of photoelectrons in the image, related with the number of Cherenkov photons produced in the showers and thus, with the energy of the primary particle.
- *Width*: Second moment of the light distribution along the minor axis of the ellipse, related with the transversal spreading of the light.
- *Length*: Second moment of the light distribution along the major axis of the ellipse, related with the longitudinal development of the shower.

- *Dist*: Measures the distance between the centroid of the elliptic image and the source position in the camera. It is related with the distance of the shower from the telescope axis.

- *Theta (θ)*: Angular distance between the position of the source and the estimated source position for an event. In the analysis, θ^2 is more commonly used, since the background distribution is approximately flat while the γ-ray distribution is exponential.

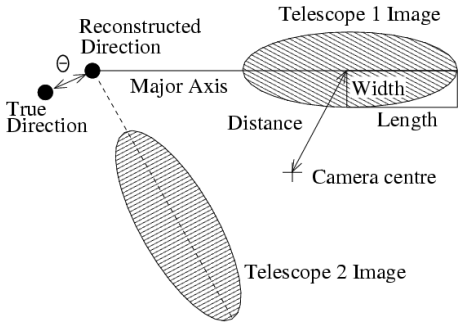

Figure 4: Definition of the Hillas parameters for a γ-ray image using two IACTs. *Credit: H.E.S.S. Collaboration* [29].

Once the shower is parametrized, the data analysis chain can be started.

3. The MAGIC Telescopes

3.1. The Telescopes

The MAGIC (Major Atmospheric Gamma Imaging Cherenkov Telescopes) Florian Goebel telescopes (see Figure 5) are two IACTs located on the Canary island of La Palma, at the Roque de los Muchachos Observatory. The first telescope, MAGIC-I (M1), is fully operative since 2004, and the second one, MAGIC-II (M2), operates since 2009. Both of them have been upgraded during 2012 and 2013 to improve stereoscopic performance. These two telescopes are one of the leading facilities for VHE astronomy, with the lowest energy threshold of all stereo IACTs, being able to detect photons above 50 GeV [30].

Each telescope is composed of an active reflective mirror surface of 236 m^2 and a diameter of 17 m. The reflective surfaces have a parabolic shape with an Active Control system that ensures optimal orientation and focusing [31]. The parabolic shape is an isochronous surface which guarantees the conservation of the arrival times. The focal length is 17 m, which gives a focal-diameter ratio of $f/D = 1$.

Both telescopes use an alt-azimuth mount in which the pointing direction varies by a movement in two perpendicular axes, one horizontal and one vertical. The structure is made of carbon fiber reinforced tubes and the whole mount moves on six bogeys placed on a circular rail of 19 m diameter. The telescopes can point anywhere in the sky in 40 s, time that can be shortened to 20 s if the fast GRB mode is active.

Figure 5: MAGIC telescopes, located at the Roque de los Muchachos observatory. *Credit: Daniel López, IAC.*

The cameras of the MAGIC telescopes are mounted on the focal plane, on an aluminium arc secured by steel cables. Both cameras are made of 1039 photomultiplier tubes (PMTs) in a circle of 1 m diameter, which provides a field of view (FoV) of 3.5^o in the sky. PMTs are used because the IACTs must be very sensitive due to the low flux received, and very fast to detect the Cherenkov flashes. Each PMT acts as a pixel, covering 0.1^o. PMTs have a peak efficiency of ∼32%, with a low gain of typically $3{\cdot}10^4$ to allow observations under moderate moonlight conditions without damaging the camera [32]. The calibration is performed by illuminating uniformly the PMTs with well characterized light pulses of different intensities with a Nd:YAG laser installed in the calibration box, in the center of each mirror dish.

Also, both telescopes are equipped with very fast readout electronics and data acquisition (DAQ) systems because of the short duration of the Cherenkov light. The DAQ software is written in C++, based on the version for MAGIC-I DAQ and improved and adapted to the new features [33].

Another important property of the telescopes is the sensitivity, defined as the flux of a source such that we obtain $N_{excess}/\sqrt{N_{off}} = 5$ after an effective observation time of 50 hours, considering also $N_{excess} > 5\%N_{off}$ and $N_{excess} > 10$ in every energy bin to avoid systematic effects on the background estimation, where N_{excess} is the number of γ-ray events detected and N_{off} is the background flux. Under these assumptions, current MAGIC sensitivity above 250 GeV is estimated to be $0.71 \pm 0.02\%$ of the Crab Nebula flux (the standard candle at VHE[3]) after 50 hours of observation (see Figure 6) [34].

In IACTs, the atmosphere acts as a calorimeter, having a strong influence in the quality of the observations due to the fast changing transparency and conditions. To monitorize and measure the atmospheric transmission, the MAGIC telescopes are equiped with a LIDAR system, acronym that stands for LIght Detection And Ranging [37]. This LIDAR technique

[3]Since Crab Nebula is the standard candle of VHE astronomy, it can be used to test the performance of the telescopes.

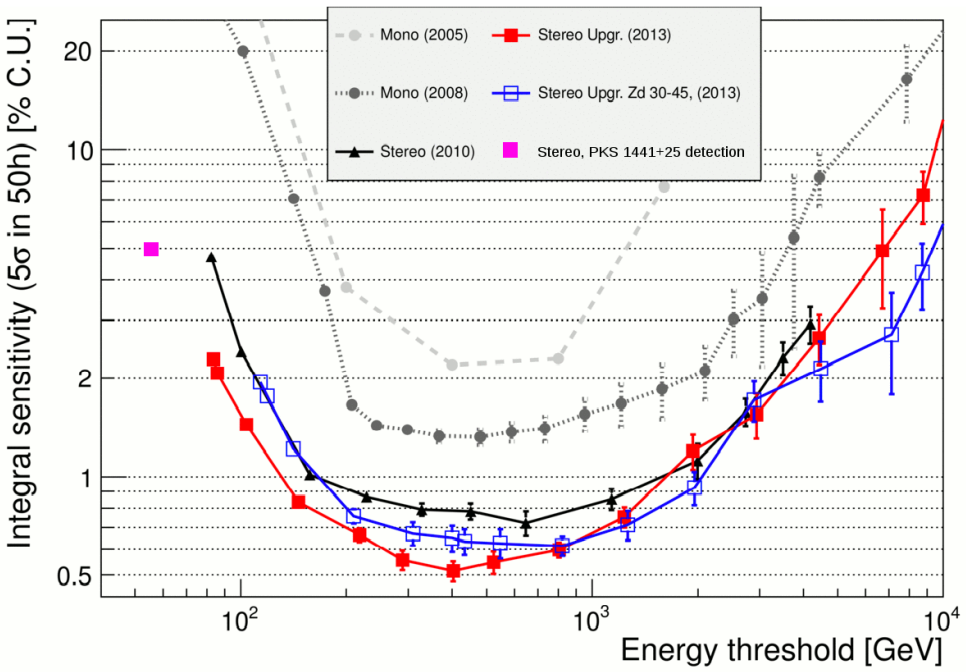

Figure 6: Evolution of the integral sensitivity of the MAGIC telescopes. *Grey circles*: Sensitivity of the MAGIC-I single telescope with the Siegen (light gray, long dashed) and MUX readouts (dark gray, short dashed). *Black triangles*: MAGIC stereo configuration before the upgrade. *Squares*: MAGIC stereo configuration after the upgrade: zenith angle below 30^o (red, filled), 30-45^o (blue, empty). The added pink point shows the integral sensitivity above 55 GeV obtained with the PKS1441+25 detection sample [35]. *Credit: Aleksić et al.* [36].

uses a short pulse monochromatic laser in the optical spectrum to determine the distance and properties of backscattering objects. The MAGIC LIDAR consists in a Nd:YAG laser emitting at 532 nm, a light collector mirror of 0.6 m diameter and a focal length of 1.5 m to collect a sufficiently large number of backscattered photons, a robotic equatorial mount that allows the alignment and tracks the observed position of the MAGIC telescopes and a detector module with a Hybrid Photo Diode (HPD) detector. The final product of LIDAR's analysis is a vertical profile of the extinction coefficient, that can be converted into a transmission profile for the aerosol component, used for all further atmospheric corrections of MAGIC data [38].

Most part of the observations performed with MAGIC are done with the called wobble mode in which the source is positioned off-axis instead of centered in the camera. Most are made with a 0.4^o displacement, however, depending on the studied source, this can change. The data analyzed in this project was taken under this observation mode and an off-axis displacement of 0.6^o, to cover a larger FoV. This wobble mode makes successive observations swapping the position of the source 90^o every 20 minutes. This allows to take simultaneously ON and OFF data. This is because the data taken with the position opposite to the source, called anti-source (for example 0^o and 180^o), and also with the other positions (typically two, 90^o and 270^o), can be used as OFF data, reducing the observation time.

3.2. Data Analysis

The main goals of the data analysis are: to confirm the detection of the source, to obtain the location and shape of the source, extract the energy spectrum and study the temporal evolution of the VHE emission with the lightcurve.

The standard software used for data analysis is MARS, acronym for MAGIC Analysis and Reconstruction Software [39]. MARS is written in C++ programming language and operates in a ROOT environment, program developed by CERN (*Conseil Européen pour la Recherche Nucléaire*, in english European Organization for Nuclear Research) [40].

In the following subsections we will provide detailed information of the event reconstruction theory and all the MARS routines used in our data reduction. The main steps of this reduction are:

- Signal extraction: reconstruction of the arrival times and the size of the Cherenkov shower.
- Event reconstruction: performed by the image cleaning and parametrization.
- Signal and background discrimination and energy estimation: by performing the γ/hadron separation.
- Signal evaluation: extraction of the skymap, lightcurve and energy spectrum of the source.

3.2.1. Low level Data Reconstruction

In the first steps of the analysis for MAGIC stereo configutarion, each telescope's data is treated separately. Once the image is parametrized, image cleaning is performed, using the information from the pixels in order to identify which ones belong to the shower and which ones are associated to the background noise. This procedure uses two different thresholds, one for determining the core pixels of the image, with a charge above a value q_1 (in terms of the number of photoelectrons), and another one for identifying all pixels with a core pixel as neighbour and a charge above q_2, with $q_1 > q_2$. Stablishing a softer or tougher cleaning level may affect in the number of pixels of the image and the level of background introduced in the data.

To complement and improve the core and boundary pixel selection, also an arrival time value is assigned to each pixel (see Figure 7). A timing coincidence window between the mean arrival time and the single pixel arrival is used to distinguish between the real image and the signal introduced by the background noise [41]. All core pixels whose arrival time is not within a time interval Δt_1 are rejected, and the same happens with boundary pixels with an arrival time higher than Δt_2. For the stereo configuration, MAGIC-I core pixels have a threshold of 6 phe and a time interval of 4.5 ns, while boundary pixels are defined by a signal of 3 phe and a time arrival within 1.5 ns. MAGIC-II thresholds are 9 phe and 4.5 phe for core and boundary pixels respectively, higher than MAGIC-I due to a higher light collection efficiency [42].

Once the image cleaning and the time arrival reconstruction are done, the image is parametrized via the Hillas parameters (see Subsection 2.3), to allow the discrimination between γ-rays and the hadronic background and estimate the energy and incoming direction of the primary event. Intermediate level and high level data reconstruction are the next steps, in which the γ/hadron separation and the energy and direction estimations are done.

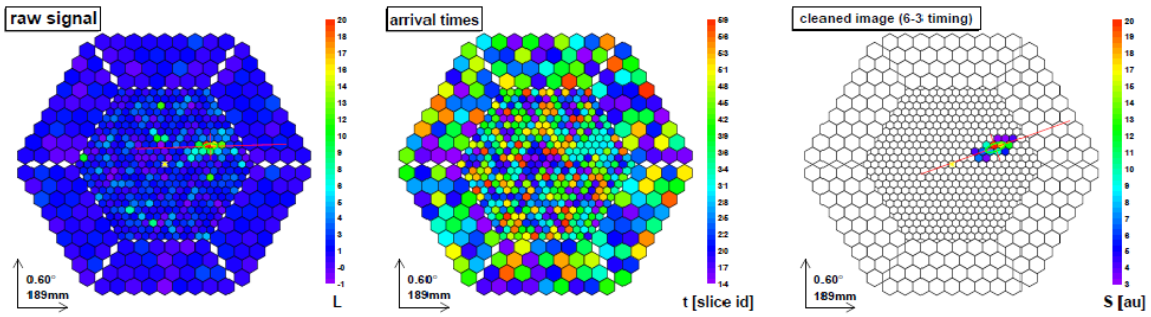

Figure 7: Image cleaning method. *Left*: Unprocessed shower image. *Center*: Arrival times. *Right*: Cleaned shower image. *Credit: E. Aliu et al.* [41].

3.2.2. Intermediate Level Data Reconstruction

In this subsection and in Subsection 3.2.3 we will describe the procedure of the data reconstruction and the MARS routines used in this project [39]. Typically, the users start the analysis with *Star* files, which are individual telescope files that contain information of the Hillas parameters for each event.

3.2.2.1 Quate

IACT data is limited by atmospheric and light conditions such as strong moonlight, clouds or aerosol presence, that can affect atmospheric transmission. This fact makes very important to correct and select high quality data. Aerosol concentration varies in short time scales, being concentrated in the first 3 km of the atmosphere, becoming one of the most important factors of atmospheric extinction via Mie scattering. The second factor that must be taken into account is Rayleigh scattering with molecules suspended in the atmosphere.

This phenomenon, joined to the fact that the Cherenkov shower development depends on the refraction index and air density, and also that part of the light is absorbed in its path to the detector, produces a blurring and dimming of the detected image, making it necessary to know the behaviour of the atmosphere and the atmospheric transmission in order to distinguish data taken under good or bad atmospheric conditions [43]. *Quate* is an executable in MARS software that performs data selection and classification according to the quality of the files, allowing the user to make a data quality selection. It is usually taken as reference for this purpose the aerosol transmission at a height of 9 km, and also cuts in the dark current (DC), zenith angle (ZA) and rate are applied to make this data selection. *Quate* uses the information of the MAGIC LIDAR, but in case that information is not available, the data provided by a pyrometer can be also used as a first approximation.

Besides from this executable, in order to crosscheck the quality selection, we have also used a ROOT/C++ script that provides information about the rate distribution in terms of ZA and DC for every individual file (see Figure 8, quality data for 2FHL J1839.5-0705). This macro permits to crosscheck the results of *Quate*, and in case that any file with high DC values or a rate excessively large or small has not been rejected by *Quate*, dircard it from the analysis.

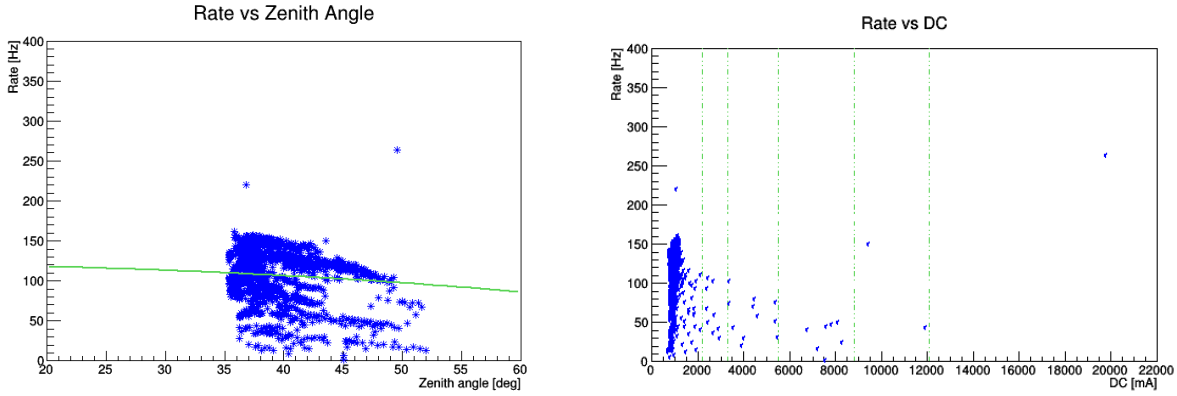

Figure 8: *Left*: Rate-ZA plot for MAGIC-I 2FHL J1839.5-0705 data. *Right*: Rate-DC plot for MAGIC-I 2FHL J1839.5-0705 data. Data before the quality selection.

A low rate value indicates a worsening of the atmospheric conditions, and a high value is a sign of an accidental increase due to stars, moonlight or car lights flashing onto the camera. The rate follows a distribution proportional to $\sqrt{\cos(ZA)}^{0.35}$ [44], so with the Rate-ZA plot we can eliminate those files whose rate value deviates more than $\pm 20\%$ from the average rate. On the other hand, the DC is related with the moonlight conditions, and since we are analyzing only dark night data, we reject all the files with DC values abnormally high. This can be easily done with the information provided by the Rate-DC plot.

3.2.2.2 Superstar

Once the bad quality data has been rejected, the stereo reconstruction takes place, which is made with *Superstar* routine. Each telescope sees the shower at a different position, but the main axis of both images points towards the incident direction (see Figure 4), being the crossing point the incident direction of the primary γ-ray. This reconstruction is very precise as long as the angle between the two axes is large enough. *Superstar* merges two single *Star* files, with individual image parameters, into a stereo image file which contains information about the reconstructed parameters, performing the steroscopic reconstruction of the shower.

Standard MAGIC analysis is optimized for point-like sources: with an extension smaller than the wobble offset and located at the camera offset. The analysis of the extended or off-centred sources differs from the standard settings after *Superstar* level. This is the case of our study.

3.2.2.3 Coach

At this level of analysis, the data contains both γ-rays and hadronic events, along with muon detections and accidental triggers due to background signal. In order to distinguish the signal of the source from the background contribution, the γ/hadron separation is done with *Coach* executable. This process leads to the definition of a parameter called hadronness, with values between 0 and 1. γ-ray images tend to a hadronness value close to 0, while hadronic shower images have values in the whole range. To estimate this parameter, a Random Forest (RF) algorithm is applied. This method creates a large number of classification trees, and is

trained with events of known nature extracted from Montecarlo (MC) simulations of "off" data (a region of the sky where no VHE emission is detected, and has been taken under similar conditions that our data sample) within a ZA range similar to our data. Each event passes through all the trees of the algorithm, and a hadronness value is asigned for each tree. The average value obtained over the N trained trees defines the final hadronness of the event, allowing to distinguish between a hadronic and a γ-ray event.

Aside from the γ/hadron separation, *Coach* and the RF algorithm are also used to perform the energy estimation and the position reconstruction. For the energy estimation of stereo data, the lookup table (LUT) method is used. These LUTs store the values of the energy and the corresponding RMS in multidimensional tables with a similar MC procedure. In regard to the position reconstruction, the DISP (Distance between the Image centroid and the Source Position) method is applied. This method uses a DISP-RF random forest to obtain the DISP parameters, and for stereo configuration, after a first estimation with geometrical reconstruction, an improved value is obtained by combining DISP results from both telescopes.

3.2.2.4 Selectmc

For the analysis, we need MCs that reflect the telescope acceptance in the region of our source. Usually we assume radial symmetry and thus, the acceptance just depends on the distance from the camera centre. In the case of extended and off-centered sources, the diffuse MCs are generated in a way that the source is randomly distributed between 0 and 1.5^o. However, since the source just fills part of the FoV, we need to select MCs that are depicting our telescope's acceptance in the same radial distance from the pointing. Hence, it is important to have an estimation of the extension of the source (in our case, we have considered 0.2^o, taken from *Fermi*-LAT 2FHL catalog [8]), that it is then applied to our MC. Also, since our data has been taken with a displacement of 0.6^o, *Selectmc* is used to correctly stablish the region in which we are going to estimate the flux later.

3.2.2.5 Melibea

The next step is to estimate the characteristics of the primary event iniciating the shower. The most important features are: nature (γ or not), energy and direction. This task is done by *Melibea*. This executable converts de Hillas parameters files produced by *Superstar*, using the RF generated by *Coach*, into fully analyzed event files, assigning a hadronness value and an energy to each event.

3.2.3. High Level Data Reconstruction

Once the *Melibea* files are produced, the final step is to extract the significance, skymaps, flux and spectrum from these data. This can be done with the high level analysis routines *Odie*, *Caspar*, *Flute* and *Unfolding*.

3.2.3.1 Odie

Odie allows the user to evaluate the On and Off event distributions with θ^2 by generating $N_{on} - \theta^2$ and $N_{off} - \theta^2$ histograms, as well as the number of γ-ray excess events with θ^2, where $N_{ex} = N_{on} - N_{off}$. The signal is determined by all the excess events within an upper θ^2 cut, while the background flux follows a flat distribution with θ^2 (see Figure 9). *Odie* also performs an estimation of the source extension and the Point Spread Function (PSF) by fitting the On-minus-Off histogram.

The other important feature of this routine is the calculation of the significance. In VHE astronomy, the reliability of a source detection is expressed in terms of the significance. For MAGIC data, the significance is defined by the Li & Ma formula [45], given by Equation (3),

$$\sigma = \sqrt{2}\left\{N_{on}\log\left[(\tau+1)\left(\frac{N_{on}}{N_{on}+N_{off}}\right)\right] + N_{off}\log\left[\left(\frac{1+\tau}{\tau}\right)\left(\frac{N_{off}}{N_{on}+N_{off}}\right)\right]\right\}^{1/2} \quad (3)$$

where N_{on} and N_{off} are the number of signal and background events in the defined region respectively and τ is the ratio of Off to On exposure. Traditionally, in γ-ray astronomy, the minimum significance value to consider a source detection is 5σ.

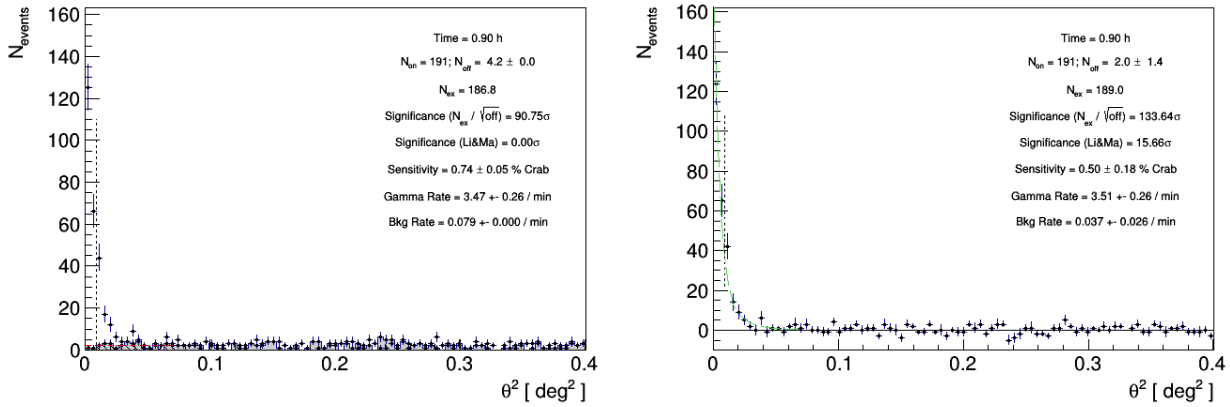

Figure 9: *Left*: On-and-Off plot of the Crab Nebula. *Right*: On-minus-Off plot of the Crab Nebula. The estimated PSF and source extension are represented by the green and red lines respectively.

3.2.3.2 Caspar

The skymap of the region is one of the essential results of the data analysis, and it is specially important in case of extended sources to study their morphology. This map is basically a significance plot that gives information about the extension and spatial distribution of the source and the arrival direction of the incoming γ-rays. *Caspar* generates the skymap of the source by transforming the reconstructed arrival directions into events in the sky, obtaining a random distribution around the true position of the source, that corresponds to the PSF. An example of an skymap of the Crab Nebula is shown in Figure 10. The TS value of the skymap corresponds to Li & Ma significance given by Equation (3).

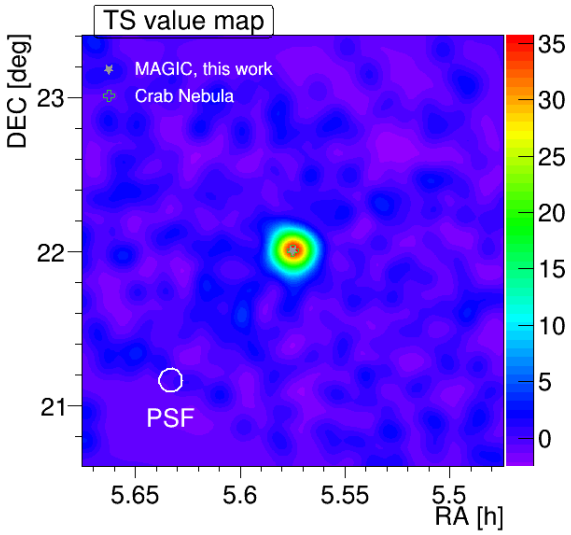

Figure 10: Skymap of the Crab Nebula.

3.2.3.3 Flute

The energy spectrum, the flux and the lightcurve (evolution of the flux with time) of the source can be obtained with *Flute* executable. The flux can be defined as the rate of γ-rays per area unit, as it is shown in Equation (4),

$$\Phi = \frac{d^2N}{dSdt}\ cm^{-2}s^{-1} \tag{4}$$

where N is the number of detected γ-rays, calculated as $N = N_{on} - N_{off}$, dt represents the effective observation time and S is the effective collection area, calculated from MC simulated events (area of an ideal device that detects 100% of the γ-rays, and detects the same rate as our instrument). From this definition of the flux, three important concepts can be calculated. The first one is the differential energy spectrum, defined in Equation (5) as the flux per interval of energy.

$$\frac{d\Phi}{dE} = \frac{d^3N}{dSdtdE}\ TeV^{-1}cm^{-2}s^{-1} \tag{5}$$

The second one is the spectral energy distribution (SED), which corresponds to the energy flux per interval of $\log(E)$, defined in Equation (6).

$$E^2\frac{d\Phi}{dE}\ TeVcm^{-2}s^{-1} = E\frac{d\Phi}{d(\log(E))} \tag{6}$$

The last important concept derived from the flux is the integral flux, given by Equation (7), which represents the total flux in a given energy range above an energy value E_{low}.

$$\Phi_{E>E_{low}\ GeV} = \int_{E_{low}\ GeV}^{\infty} \frac{d\Phi}{dE}dE\ cm^{-2}s^{-1} \tag{7}$$

With the integral flux, we can define the lightcurve as the evolution of the integral flux over time in a certain energy range. Figure 11 shows the differential energy spectrum and the SED of a sample of Crab Nebula data, taken under similar conditions that our source of study to check the proper performance of the instruments.

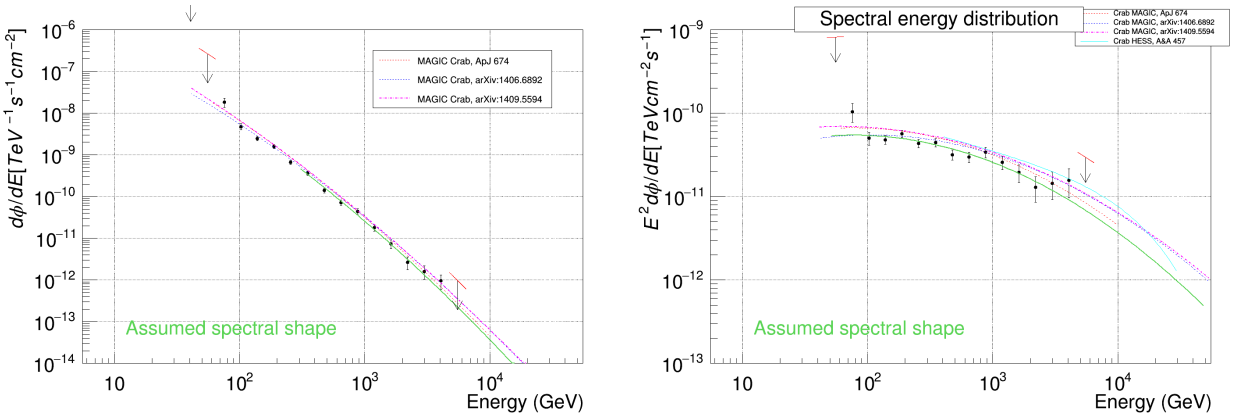

Figure 11: *Left*: Differential energy spectrum of the Crab Nebula. *Right*: Spectral energy distribution of the Crab Nebula.

3.2.3.4 Unfolding

The goal of the *Unfolding* [46] is to estimate the true energy spectrum of the source, since the parameters and the estimated energy E_{est} derived from the LUTs have a finite resolution. The detection of a source suffers from several issues like limited acceptance since not all the γ-rays entering the atmosphere are detected by the telescope, and due to the interactions of these γ-rays with the molecules in the air, it is not possible to detect them directly from Earth. The energy estimation has a limited resolution of around a 15% in the case of the MAGIC telescopes. The *Unfolding* method solves all these problems by transforming the distribution of an observable (E_{est}) into a true distribution of a physical quantity (E_{true}). Mathematically, the method is described by the Fredholm integral equation shown in Equation (8),

$$g(y) = \int_c^d M(x,y) f(x) dx + b(y) \tag{8}$$

where $g(y)$ and $f(x)$ represent the distribution of E_{est} and E_{true} respectively, $M(x,y)$ is the response function or migration matrix obtained by MC simulations and $b(y)$ takes into account the background distribution. We will search for an agreement of the different methods applied. The most simple way to resolve Equation (8) is via Forward unfolding, where the spectral shape is assumed to be an analytical function, and the result is not a series of spectral points, but the parameters of that function. The other methods will use different algorithms that will provide the real spectral points.

The *Unfolding* is performed by the Unfold routine and the CombUnfold.C macro, with different unfolding algorithms. An example of an unfolded spectrum is shown in Figure 12.

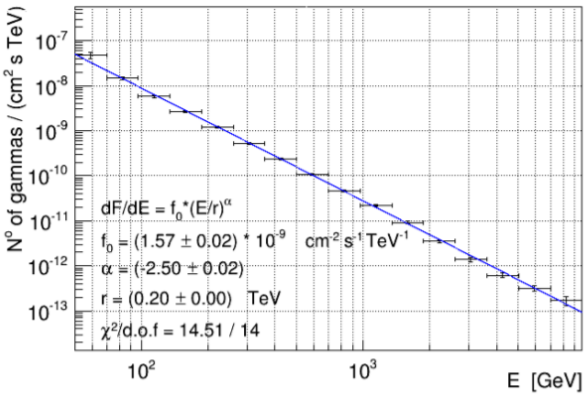

Figure 12: Unfolded spectrum of the Crab Nebula. *Credit: G. Gumiero* [47].

4. Unidentified Fermi Object (UFO): 2FHL J1839.5-0705

4.1. UFO 2FHL J1839.5-0705 and Region G25

2FHL J1839.5-0705, located at α=18h 39' 30.2" and δ=-07^o 05' 34.8", is an unidentified weak source in the galactic plane. It was first detected by *Fermi*-LAT up to 500 GeV and included in the 2FHL catalog (the second catalog of hard *Fermi*-LAT sources, with more than 360 detected objects) [8]. It does not show any counterpart at other wavelengths.

This source lies in a very rich complex region, known as G25. This region is thought to be a SFR, potentially powered by the presence of a hidden massive OB star/cluster. This OB association is not detected in optical due to the heavy extinction, but 8 μm emission is observed [48]. Also, a possible counterpart to this OB cluster/association has been identified in X-rays, G25.18+0.26 [49]. This region also shows bubble-like structures of atomic and molecular gas (similar to those found in Cygnus Cocoon) which are likely created by this OB complex. SFRs can be sites of γ-ray production, if particles are accelerated efficiently via wind energy [50].

G25 region, with coordinates α=18h 36' 24" and δ=-06^o 42' 00", covers an area of $\sim$1.5^o, with an extended main source called HESS J1837-069, detected in the TeV range and thought to be a PWN [51]. This source has an elongated shape modeled as three Gaussian components, with an extension of 0.36^o $\pm$ 0.03^o, being coincident with the southern part of the G25 region in hard X-rays. This region also contains:

- Three sources from *Fermi*-LAT Second Source Catalog 2FGL: 2FGL J1835.5-0649 and 2FGL J1837.3-0700c, which are two possible counterparts at TeV and 10-100 GeV energies respectively [52]; and 2FGL J1836.6-0623c, a point source near HESS J1837-069 [49].
- Two possible pulsars/PWN detected at keV energies: AX J1838.0-0655, a bright point source possible counterpart of HESS J1837-069 surrounded by a 2' diameter nebula, and AX J1837.3-0652, that may also contribute to HESS J1837-069 [53].
- Three counterpart sources to HESS J1837-069 from HAWC catalogs, detected at TeV energies: 2HWC J1837-065 [54], 1HWC J1838-060 and 1HWC J1836-074c [55].

- Three sources detected in several catalogs such as FGES (*Fermi*-LAT Galactic Extended Source catalog), 2FHL or 2FGL: 2FHL J1837.4-0717; and two of them related with the star-forming region, 2FHL J1836.5-0655e, which is thought to be a PWN or a SFR, and 2FHL J1839.5-0705 [8].

The main sources in the region G25 detected by different observatories and telescopes such as HAWC, H.E.S.S. or *Fermi*-LAT are shown in Table 1.

Name	Position (RA [h], Dec [^{o}])	Type[1]	Energy range[1]	Counterpart/ association
HESS J1837-069	(18.6273, -6.9500)	PWN	TeV	-
2FHL J1839.5-0705	(18.6539, -7.0547)	SFR?	GeV	-
2FGL J1835-0649	(18.5933, -6.8312)	?	GeV	HESS J1837-069
2FGL J1836.8-0623c	(18.6147, -6.3860)	?	GeV	-
2FGL J1837.3-0700c	(18.6232, -7.0109)	PWN or SFR	GeV	HESS J1837-069
AX J1838.0-0655	(18.6342, -6.9259)	Pulsar+PWN	keV	HESS J1837-069
AX J1837.3-0652	(18.6226, -6.8752)	Pulsar+PWN	keV	-
1HWC J1836-074c	(18.6067, -7.4000)	?	TeV	HESS J1837-069
1HWC J1838-060	(18.6400, -6.0000)	?	TeV	HESS J1837-069
2HWC J1837-065	(18.6240, -6.5800)	?	TeV	HESS J1837-069
2FHL J1836.5-0655e	(18.6095, -6.8660)	PWN or SFR	GeV	2FHL J1839.5-0705
2FHL J1837.4-0717	(18.6242, -7.2964)	?	GeV	-

[1]Extracted from the Supernova Remnants catalog of the Department of Physics and Astronomy of the University of Manitoba (*Gilles Ferrand & Samar Safi-Harb* [56] [57]).

Table 1: Main sources of region G25.

4.2. MAGIC Observations

In order to search for γ-ray emission from 2FHL J1839.5-0705, we have a total of 30.3 hours of observations taken with the MAGIC telescopes during year 2017 in three different periods: June 18th to June 30th, July 15th to July 25th and August 18th to August 25th.

These data were taken with 4 custom wobble positions, W0.60+045/225 and W0.60+135/315 and an off-axis displacement of 0.6^o to cover a larger region of the sky. This allows to have a wider area without contaminating γ-ray emission (to properly estimate the background) and also to study most of the sources in the vicinity. The observations were taken under dark conditions due to the weakness of the source. The zenith angle range used in the observations goes from 35 to 50 degrees.

Table 2 shows the total and effective times before and after the data quality selection in a daily basis. A summary of the total amount of data is collected in Table 3. For this selection, we distinguished those days in which LIDAR information was available from those in which it was not, stablishing a transmission cut at 9 km of 0.65 for data containing LIDAR information and 0.85 for those days where this information is missing. Also, a duration cut for exposures shorter than 10 s has been used, and for those days without LIDAR, we used the pyrometer data to reject days with cloudy weather. Finally, data with an abnormal rate (either too high

due to i.e. car flashes or too low due to clouds or strong calima) value was rejected with the macro mentioned in Subsection 3.2.2.1.

Day	MJD[1]	$t_{total}(h)$	$t_{eff}(h)$	Day	MJD[1]	$t_{total}(h)$	$t_{eff}(h)$
18/06[2]	57922	0.5	0.48	15/07	57949	1.5	1.33
19/06[2]	57923	0.7	0.64	17/07	57951	1.8	0.39
20/06[2]	57924	1.5	1.48	18/07	57952	1.6	1.57
21/06[2]	57925	1.0	0.98	19/07	57953	1.4	1.34
22/06[2]	57926	1.0	0.18	20/07	57954	1.7	1.61
23/06[2]	57927	0.8	0.10	23/07	57957	1.6	1.60
24/06[2]	57928	0.8	0.07	24/07[2]	57958	1.6	1.60
25/06[2]	57929	1.0	0.18	25/07	57959	1.6	1.45
26/06[2]	57930	1.0	0.17	18/08	57983	1.2	1.19
27/06[2]	57931	0.8	0.66	19/08	57984	1.7	1.62
28/06	57932	1.3	1.29	21/08	57986	0.6	0.46
29/06	57933	1.0	0.93	24/08	57989	1.3	1.28
30/06	57934	0.5	0.49	25/08	57990	1.5	1.45

[1]Modified Julian Day.
[2]Days with LIDAR data not available.

Table 2: Daily total and effective observation hours.

$t_{total}(h)$	$t_{eff}(h)$
30.30	24.52

Table 3: Total and effective observation hours from 57922 MJD to 57990 MJD.

4.3. Results and Discussion

4.3.1. Region Morphology and Position Fit

Before analyzing the characteristics of 2FHL J1839.5-0705, it is important to understand the morphology of the G25 region because of all the VHE sources lying in it. For this purpose, we have made a skymap with all the sources considered in Table 1 that will help us to distinguish our weak source from all the bright sources in the surroundings. This is also necessary to define a procedure on how to estimate the best solutions to detect our source and avoid contamination from other TeV sources. This skymap, made with *Caspar* executable, is represented in Figure 13.

We have also performed a position fit which we can use to determine the coordinates of 2FHL J1839.5-0705 with precision. We have compared the position obtained with this MAGIC analysis with the one extracted from 2FGES [58] and 2FHL [8] *Fermi*-LAT catalogs. The results are shown at Table 4.

We can see that the performed position fitting is compatible with the position derived from the *Fermi*-LAT catalogs. This indicates that the emission detected by *Fermi*-LAT and MAGIC come from the same region and it is most likely associated.

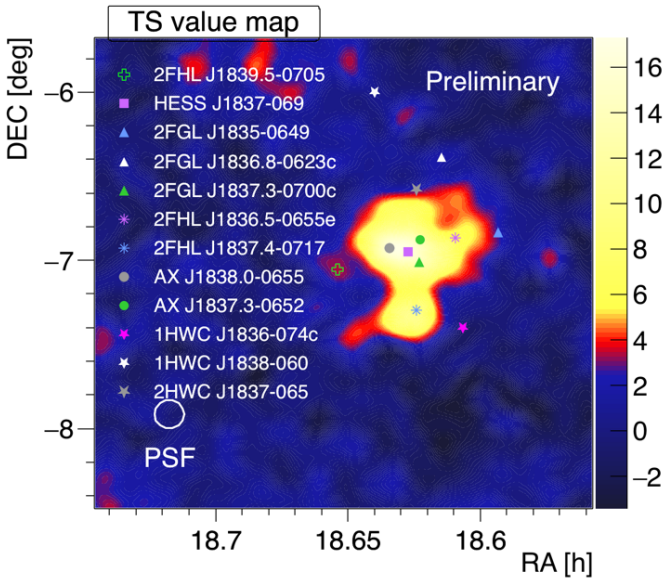

Figure 13: Skymap of the region G25 with all the considered sources for $E > 250$ GeV. Our source of main interest, 2FHL J1839.5-0705, is located at the center of the region.

	RA (h)	Dec (^{o})
MAGIC	18.6517 ± 0.0007	-7.0770 ± 0.0163
2FHL	18.6584 ± 0.0800	-7.0843 ± 0.0800
2FGES	18.6497 ± 0.0018	-7.0670 ± 0.032

Table 4: Fitted position for 2FHL J1839.5-0705.

Besides the skymap presented in Figure 13, we have produced skymaps at other energies to understand how the emission and morphology of the region change. We obtained the low energy (LE, $E > 100$ GeV), full range (FR, $E > 250$ GeV) and high energy (HE, $E > 1$ TeV) skymaps centered at the 2FHL J1839.5-0705 position, and represented in Figures 14, 15 and 16. We have generated two types of skymaps: a first type optimized for the source detection, maximizing the significance value; and a second one in which a smearing kernel was used, decreasing the significance but allowing us to distinguish the different sources in the region.

For this purpose, is importat the choice of the total PSF, which can be estimated as:

$$\sigma_{total} = \sqrt{\sigma^2_{MAGIC} + \sigma^2_{kernel}} \tag{9}$$

where σ_{MAGIC} is the election of the PSF and σ_{kernel} corresponds to the smearing kernel. Because of Nyquist theorem, the minimum σ_{kernel} value with physical meaning is $\sigma_{MAGIC}/2$. It is important to notice that, when a kernel is not specified, the default value used by *Caspar* is $\sigma_{kernel} = \sigma_{MAGIC}$. Hence, when we define a kernel, the total PSF is smaller and we are able to distinguish more structures.

The PSFs and smearing kernels chosen for this analysis in each energy range are collected in Table 5. The selection of the PSF values are made in the way that significance takes a value as higher as possible when the kernel is not used, to increase the possibilities of detecting the source. Kernel values were selected to distinguish as many substructures as possible.

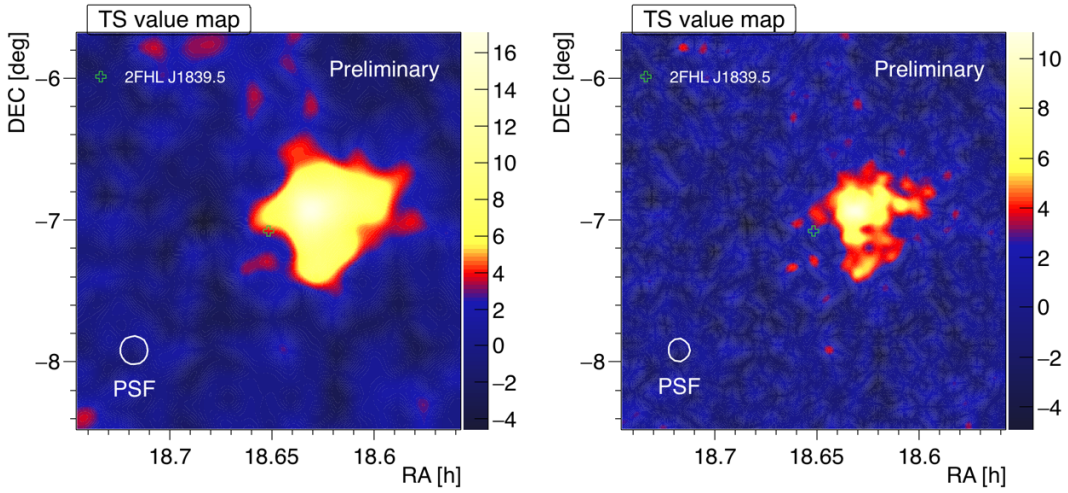

Figure 14: *Left*: LE skymap without smearing kernel. *Right*: LE skymap using smearing kernel.

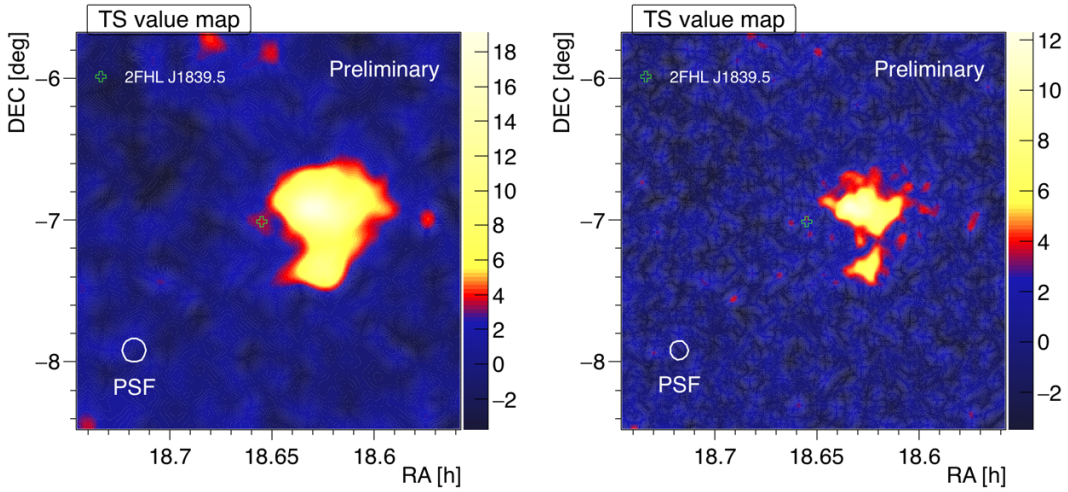

Figure 15: *Left*: FR skymap without smearing kernel. *Right*: FR skymap using smearing kernel.

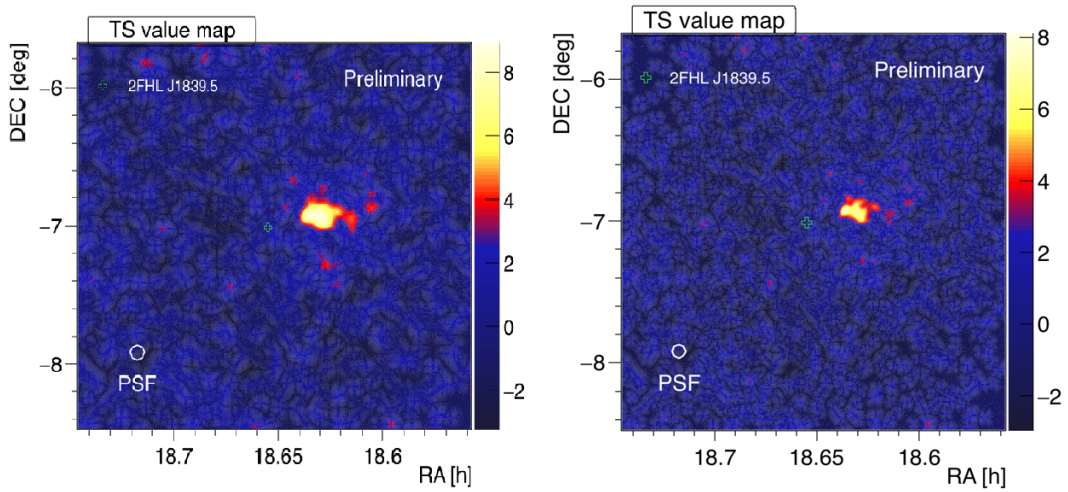

Figure 16: *Left*: HE skymap without smearing kernel. *Right*: HE skymap using smearing kernel.

The cross marked in these plots corresponds to the fitted position of 2FHL J1839.5-0705 presented before. Clearly, all images on the left are optimized to maximize the significance value while those on the right (the ones in which the smearing kernel was used), allow us to separate the sources of the region and distinguish the different structures.

At LE, a hotspot slightly shifted from 2FHL J1839.5-0705 position can be identified, which can suggest that the emission at lower energies can be displaced. This emission could be contamined by the nearby source HESS J1837-069. From the LE smeared map, we determine the hotspot's position at (18.6504, -6.9497) in (RA, Dec) coordinates, with a significance value of 4.26σ, which could be compatible with 2FHL J1839.5-0705 position. In FR, we detect a 3.46σ hotspot on the position of 2FHL J1839.5-0705. As we go to higher energies, the detection of 2FHL J1839.5-0705 becomes more difficult, becoming imperceptible at 1 TeV.

We can also crosscheck the significance value of the skymaps with the value of the significance that will present in Subsection 4.3.2, obtained with *Odie*. For the skymap, it is important to notice that, in our observations, two wobble positions are located on the bright source next to 2FHL J1839.5-0705, leading to an overestimation of the background flux and thus, to an incorrect estimation of the total excess events, which affects the significance value. *Caspar* cannot reject the background estimation from the wobble positions located on the nearby bright source, so in this case, the significance value can be slightly smaller that the one obtained from *Odie*, but is useful to detect the position of the hotspots corresponding to 2FHL J1839.5-0705 to compare it with the fitted position. The significance of the hotspots, taken from the non-smeared maps, along with their coordinates, are presented in Table 5.

Energy range	PSF	Kernel	Hotspot position (RA (h), Dec (^{o}))	Significance
LE	0.071	0.0355	(18.6516, -7.0169)	5.59
FR	0.060	0.0300	(18.6553, -7.0204)	3.46
HE	0.043	0.0300	(18.6522, -7.0685)	2.66

Table 5: σ_{MAGIC} and σ_{kernel} values for *Caspar* skymaps, with the corresponding hotspots for all energy ranges.

The difference between the positions of each hotspot it due to the fact that, at different energies, the source can change its γ-ray morphology. The emission at 100 GeV and at 1 TeV can be different because of the extension of the source and the different acceleration mechanisms. The fitted position at different energies is compatible with the position from the catalog.

Regarding the significance value, at lower energies we reach the minimum significance value to consider a source detection, while at higher energies the significance decreases. This suggests that we will not be able to detect it at HE. However, the calculation of this significance cannot be taken as a reference to confirm the detection of the source because of the overestimation of the background flux, which affects the significance computation. For a firm detection confirmation, we shall rely on the standard deviation value calculated in *Odie*.

4.3.2. Source Detection

To confirm the detection of 2FHL J1839.5-0705, we have performed a significance analysis, defined by Equation (3), by evaluating the On-Off event distribution of the region. As we

mentioned in Subsection 3.2.3.3, in order to confirm the detection of a source, the minimum significance value needed is 5σ.

We have made the significance analysis for the three cases considered before (LE, FR and HE) to understand the behaviour of the source in all the energy range in which MAGIC works. Figure 17 shows the On-minus-Off histograms for the LE, FR and HE analysis. For each energy range, we previously made an optimization of the parameters such as the PSF, which takes a higher value for lower energies due to the higher amount of γ-rays received.

As commented on Subsection 4.3.1, the source was observed using a 4-wobble configuration, but two of them are located in the position of a very bright source, HESS J1837-069. The inclusion of these two wobbles in the analysis will cause an overestimation of the background flux and the total excess events. In order to correct this effect, we have performed the background estimation only with the two wobbles located far away from the extended source (W0.60+45 and W0.60+315), improving significantly the significance of the analysis. The significance at different energies at the position of 2FHL J1839.5-0705 is shown at Figure 17.

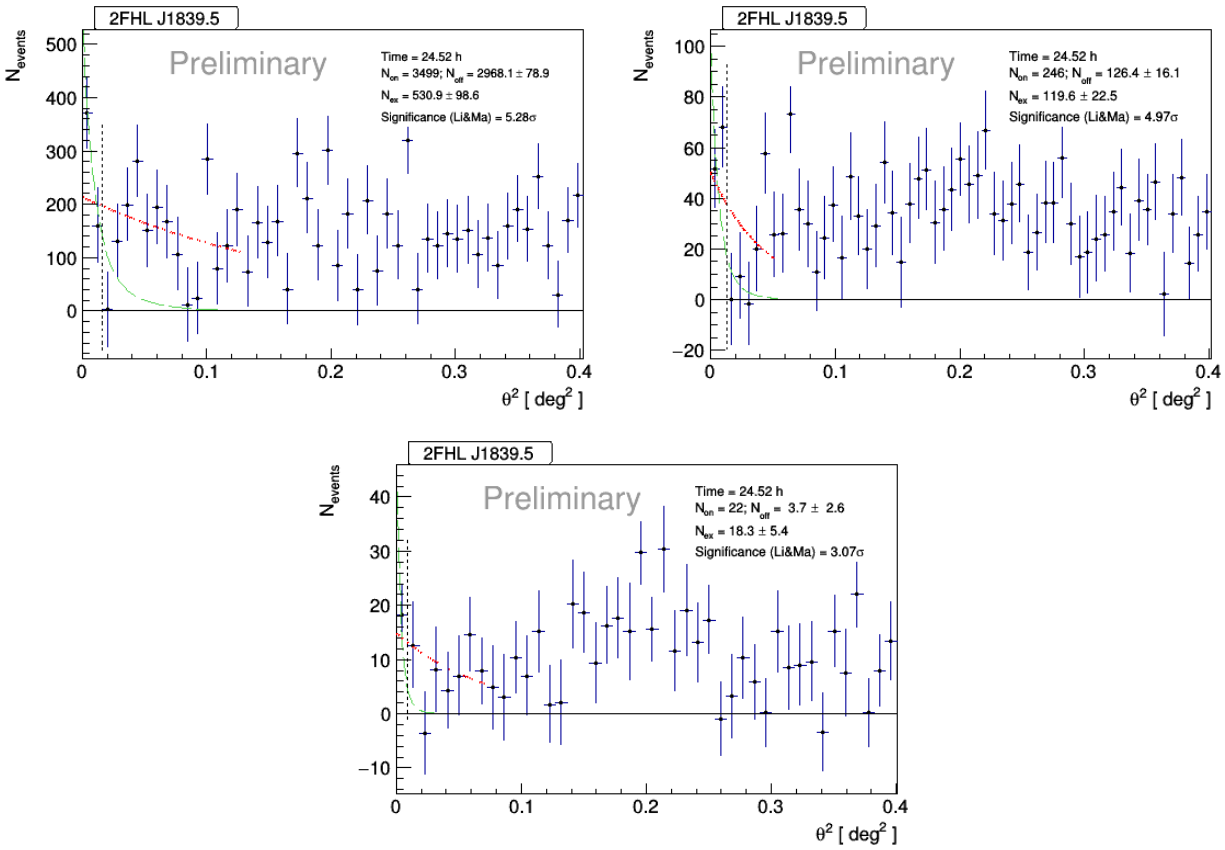

Figure 17: On-minus-Off histograms for 2FHL J1839.5-0705 source. *Top Left*: LE histogram. *Top Right*: FR histogram. *Bottom*: HE histogram. Green and red curves represent the chosen PSF and the source extension fit respectively.

The PSF values for each energy range, along with the θ^2 upper cut values in which the excess events are calculated and the significance obtained, are shown in Table 6. As it happened in Subsection 4.3.1, the PSF value will be smaller as we go to higher energies.

Energy range	PSF	θ^2 cut	Significance
LE	0.089	0.0161	5.28
FR	0.065	0.0136	4.97
HE	0.045	0.0091	3.07

Table 6: PSF, θ^2 cut and significance values for *Odie* analysis at three different energies.

Similarly to the significance maps obtained in Subsection 4.3.1, the signal is higher for smaller energies, making easier to detect the source at LE and FR energy ranges. Comparing Tables 5 and 6 we can notice that σ values are higher in the analysis performed with *Odie*, except for the case of LE. This is because the two wobble positions rejected due to their location: despite of improving the background estimation, we lose more signal than in the case of FR and HE energy ranges due to the contamination of other bright sources in the FoV, which is higher at low energies. This causes a decrease in the significance. However, we detect 2FHL J1839.5-0705 at LE at 5.28σ and we are at the limit of detection at E>250 GeV, with a significance of 4.97σ. If its nature is confirmed, this would be the first SFR detected in VHE with the MAGIC telescopes and the second one detected in the northern hemisphere. At HE, a hint of emission at the level of 3σ is detected, but it is compatible with statistical fluctuations of the background. Also, we can see from Table 5 that the PSF values that optimize the significance are similar to those used for *Caspar* skymaps.

From Figure 17 we can notice large background fluctuations. Even after discarding the two wobble positions mentioned before, the source still lies in a very complex region with multiple VHE sources, making the background estimation very difficult. To improve this, we have used a normalization option from *Odie* executable which allows to normalize the background level from the plots as far as possible to improve the analysis. Despite using this option, and due to the strong contribution from the other extended bright sources in the region, we could not eliminate completely this fluctuations.

Finally, we can perform an extension fit, which is represented by the red line in Figure 17. However in our case, the fit is affected by strong background fluctuations, due to the presence of other bright sources in the FoV. The fitted extension, which shall be taken as a preliminar value, is presented in Table 7.

Energy range	Extension (^{o})	$\Delta_{extension}$ (^{o})
LE	0.297	0.103
FR	0.135	0.070
HE	0.183	0.106

Table 7: 2FHL J1839.5-0705 extension fit and its errors extracted from *Odie* analysis.

4.3.3. Lightcurve

We can derive the lightcurve of 2FHL J1839.5-0705 during the observation period using *Flute*. The curve represents the evolution of the integral flux above a certain energy value E_{low} with time. We have analyzed the variation of the flux above different energy thresholds (200 GeV, 300 GeV, 400 GeV, 700 GeV and 1 TeV), so that we can compare our results with other observations, such as *Fermi*-LAT. We have generated lightcurves by calculating the daily (to

check for short timescale variability), monthly and total integral flux (see Figures 18, A.1, A.2, 19 and A.3).

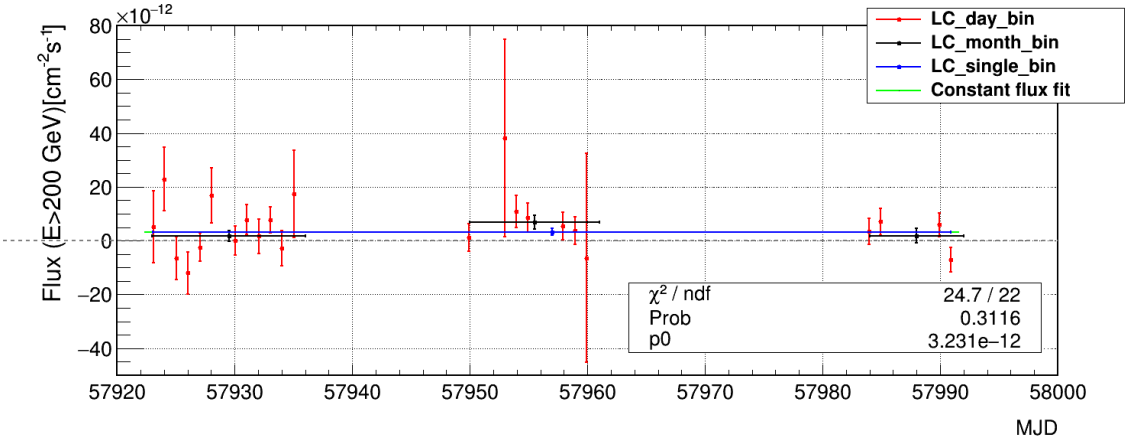

Figure 18: Lightcurve above 200 GeV. *Red*: Day-by-day integrated flux. *Black*: Monthly integrated flux. *Blue*: Total integrated flux. *Green*: Fitted line for constant integrated flux.

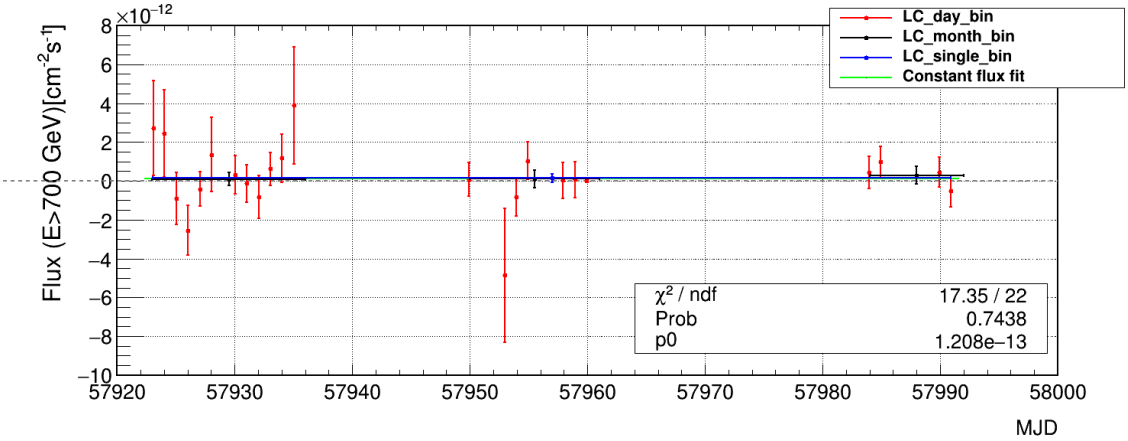

Figure 19: Lightcurve above 700 GeV. *Red*: Day-by-day integrated flux. *Black*: Monthly integrated flux. *Blue*: Total integrated flux. *Green*: Fitted line for constant integrated flux.

By analizing the figures presented before (and those in the Appendix A), we only detect some significant flux emission from 2FHL J1839.5-0705 up to 400 GeV, while for E>400 GeV, the emission is compatible with zero, which is in agreement with the skymaps obtained in Subsection 4.3.1. The large uncertainties are due to the low statistics.

We do not detect flux variability in a daily nor a monthly basis. We can check whether the detected fluxes can be a statistical fluctuation of a constant flux by fitting the overall emission to a constant function, which is represented by the green line in these plots. Table 8 contains the fit probabilities for these constant functions, which are high enough to claim that there is no flux variation in 2FHL J1839.5-0705 in the measured period. As expected (according to the skymaps obtained in Subsection 4.3.1), the received flux is smaller at higher energies, and these results are in agreement with the flux integrated by *Flute* during the whole observation period. The small probability of the fit at 200 GeV is introduced due to the fluctuations of the flux, specially during the first two months of observation. Despite this variabilities, the flux is still compatible with a constant function.

Lightcurve energy (GeV)	Integral flux ($cm^{-2}s^{-1}$)	Fitted flux ($cm^{-2}s^{-1}$)	Probability
200	$3.25{\cdot}10^{-12} \pm 1.28{\cdot}10^{-12}$	$3.23{\cdot}10^{-12}$	0.3116
300	$6.40{\cdot}10^{-13} \pm 6.58{\cdot}10^{-13}$	$8.53{\cdot}10^{-13}$	0.7256
400	$5.30{\cdot}10^{-13} \pm 4.41{\cdot}10^{-13}$	$4.19{\cdot}10^{-13}$	0.8763
700	$1.47{\cdot}10^{-13} \pm 2.24{\cdot}10^{-13}$	$1.21{\cdot}10^{-13}$	0.7438
1000	$5.71{\cdot}10^{-14} \pm 1.55{\cdot}10^{-14}$	$3.10{\cdot}10^{-14}$	0.9565

Table 8: Fitted flux and probability assuming no flux variability over time.

4.3.4. Spectrum and SED

The final step of the analysis is the extraction of the differential energy spectrum and the SED of the source. We have assumed that the differential energy spectrum can be fitted by a power law, following Equation (10):

$$\frac{dF}{dE} = f_0 \cdot \left(\frac{E}{r}\right)^{\alpha} \; TeV^{-1}cm^{-2}s^{-1} \tag{10}$$

f_0 is the differential flux normalization at the energy indicated by the normalization constant r, E represents the energy and α is the spectral index. We have performed the Unfolding (see Section 3.2.3.2 for a detailed explanation) with four different methods: Forward, Bertero, Tikhonov and Schmelling. The obtained result is presented in Figure 20, along with the SED (defined by Equation (6)).

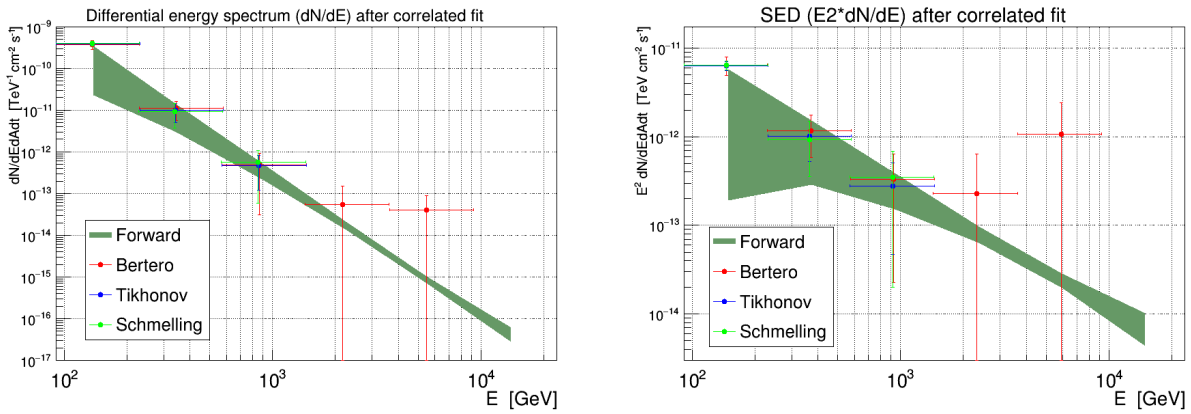

Figure 20: Differential energy spectrum (left) and spectral energy distribution (right) of 2FHL J1839.5-0705. The spectral points have been fitted with different methods: Bertero (red), Tikhonov (blue) and Schmelling (light green). The dark green butterfly is the spectral fit obtained with the Forward method.

All four methods give compatible results, with flux values between $\sim 10^{-9}$ for low energies and $\sim 10^{-13}$ for energies above $\sim$1 TeV, and compatible spectral indexes ($\alpha \sim$ -3.5). The big uncertainties visible in the last points of Bertero method appear due to the low flux received at high energies, making the detection of the source and the calculation of the flux very difficult. For even higher energies, we are unable to determine the flux due to the low statistics. Table 9 shows the fitted parameters for the most robust method, Forward unfolding. The parameters obtained with the other three methods are compatible with the results of this one, as shown in

Figure 20. The last two points in the spectrum obtained with Bertero show large uncertainties and are not significant. For our study, we will only consider the energy points between 100-1000 GeV, since those are in agreement in the three methods considered. The spectral fit is given by the Forward method. Tikhonov and Schmelling results are very similar, since both of them use a similar fitting algorithm.

Method	f_0 ($TeV^{-1}cm^{-2}s^{-1}$)	r (TeV)	α	χ^2/d.o.f.[1]	Fit probability
Forward	$(2.49 \pm 1.78)\cdot 10^{-13}$	1.00 ± 0.00	-3.31 ± 0.46	1.25/5	0.9399

[1]Degrees of freedom.

Table 9: Fitted power law parameters of the Forward method.

We can also compare the flux value of the spectrum presented in Figure 20 with the Crab Nebula spectrum shown in Figure 12. This comparison helps to notice how faint 2FHL J1839.5-0705 is, since there is a difference of four orders of magnitude between Crab Nebula's flux and the flux coming from 2FHL J1839.5-0705, something that we can also see with the value of the differential flux normalization f_0 at 1 TeV. While our source's f_0 value is $\sim 10^{-13}$ $TeV^{-1}cm^{-2}s^{-1}$, the Crab Nebula has a normalization flux of $1.57\cdot 10^{-9}$ $TeV^{-1}cm^{-2}s^{-1}$.

2FHL J1839.5-0705 is an UFO which has an unidentified nature, hence, it is important to build an SED throughout all the electromagnetic spectrum, to try to identify possible counterparts. We have searched for associated emission at other wavelenghts, but we have only found data from *Fermi*-LAT 2FHL catalog [8] and 2MASS catalog [59]. The complete SED is shown in Figure 21. The VHE SED obtained with MAGIC is compatible with that of *Fermi*-LAT, within errors. 2FHL J1839.5-0705 has not been detected in X-rays, UV and optical, in this last case due to the heavy extinction in the region G25 [49].

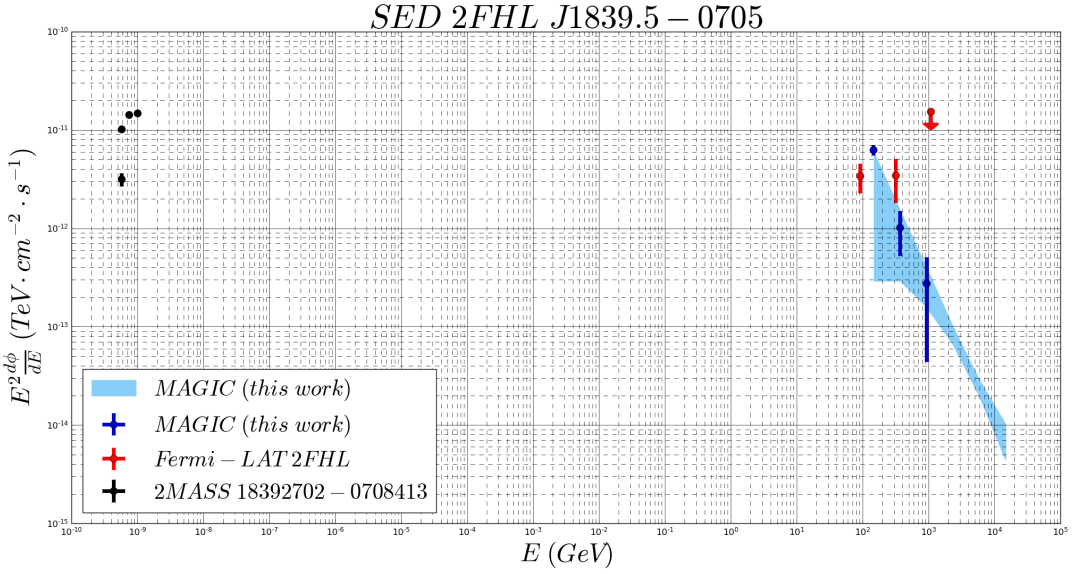

Figure 21: Spectral energy distribution of 2FHL J1839.5-0705. *Light Blue*: MAGIC telescopes (Forward method). *Dark Blue*: MAGIC telescopes (Tikhonov method). *Red*: 2FHL catalog. *Black*: 2MASS catalog.

Extended infrared (IR) emission was detected in the whole region G25. At the position of 2FHL 1839.5-0705, compatible with the fitted extension value (see Subsection 4.3.1), we

find the IR source 2MASS 18392702-0708413. This emission could be an IR counterpart to 2FHL J1839.5-0705. From 2MASS infrared catalog data, we can confirm the detection of IR radiation, more specifically, in the J, H and K bands (1220 nm, 1630 nm and 2190 nm of central wavelength respectively), coming from this 2MASS object. Besides from this detection, *Rahman & Murray* [60] claim for a large detection of 8 μm emission in this region.

This IR emission has a great importance in the determination of the nature of the source, since it could be an indicative that the source is a SFR. These regions are very opaque to be detected in optical, but IR lines associated with star-forming processes can be observed. In the early stages of a SFR, gas and dust are very cold, and therefore, they mainly emit at IR. When a massive star is formed, it heats the dust and ionizes the gas and clouds in the surroundings, causing both to radiate strongly in IR [61]. Also, jets produced in protostellar disks are observed in these wavelengths [50]. More IR observations could help to finally clarify if 2FHL J1839.5-0705 is a SFR or not.

Katsuta et al. [49] also reported ^{13}CO emission due to the presence of molecular clouds in the whole G25 region. ^{13}CO lines at v=45-64 km s^{-1} are detected at the position of 2FHL J1839.5-0705 (see Figure 22)[4]. These molecular clouds could also help to accelerate the particles in the medium via proton-proton collisions, and contribute to the detected GeV-TeV emission. This ^{13}CO emission can also be an indicator of the bubble structure commented before.

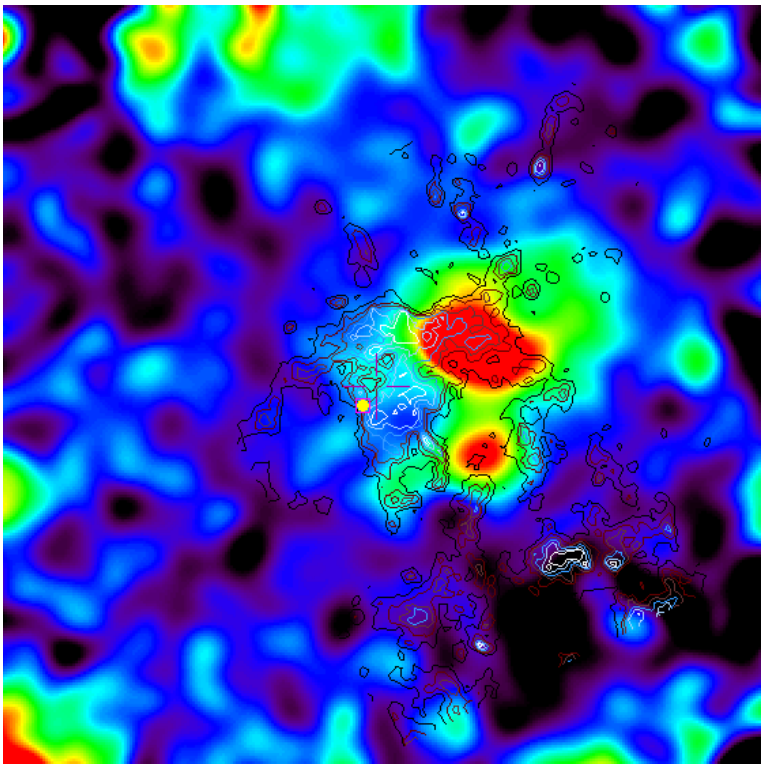

Figure 22: ^{13}CO emission contours at v=56.5 km s^{-1}. Darker lines represent a higher emission. The skymap is centered at the position of 2FHL J1839.5-0705. The yellow circle shows the position of the possible IR counterpart 2MASS 18392702-0708413.

[4]This publication makes use of molecular line data from the Boston University-FCRAO Galactic Ring Survey (GRS). The GRS is a joint project of Boston University and Five College Radio Astronomy Observatory, funded by the National Science Foundation under grants AST-9800334, AST-0098562, AST-0100793, AST-0228993, & AST-0507657 [62].

4.3.5. Comparison With Other Star-Forming Regions

A SFR consists in a concentration of cold interstellar gas (∼10-20 K) and molecular clouds composed mainly by hydrogen and helium. Those parts with a higher density collapse by the attraction of matter from the surroundings, giving place to the fragmentation of the cloud, and eventually, to protostars. The presence of an OB cluster and bubble structures are potential accelerators of particles, and γ-rays can be produced.

We can contrast our results with other known SFRs such as Cygnus Cocoon, Westerlund 1 and 2 or 30 Doradus. For this purpose, we will compare characteristics like the spectral index or the energy range in which they were detected. This comparison is presented in Table 10.

SFR	Telescope	Energy detection range	Spectral index α
2FHL J1839.5-0705[a]	*Fermi*-LAT	20 MeV-500 GeV	-2.11 ± 0.04_{stat}± 0.05_{sys}[1]
2FHL J1839.5-0705	MAGIC	50-1000 GeV	-3.31 ± 0.46
Westerlund 1[b]	H.E.S.S.	⩾100 GeV	-2.19 ± 0.16_{stat}± 0.1_{sys}
Westerlund 2[c]	H.E.S.S.	⩾100 GeV	-2.53 ± 0.08_{stat}± 0.2_{sys}
Cygnus Cocoon[d]	*Fermi*-LAT	100 MeV-100 GeV	-2.20 ± 0.1
Cygnus Cocoon[e]	ARGO-YBJ	200 GeV-10 TeV	-2.60 ± 0.30
30 Doradus[f]	*Fermi*-LAT	200 MeV-20 GeV	-1.96 ± 0.25_{stat}± 0.02_{sys}

REFERENCES: (a) *Katsuta et al.* [49], (b) *Abramowski et al.* [17], (c) *Lemoine-Goumard et al.* [18], (d) *Aharonian et al.* [16], (e) *Bartoli et al.* [63], (f) *Abdo et al.* [21].

[1]Spectral index of the entire G25 region.

Table 10: Spectral features of some of the known star-forming regions.

When analyzing the spectral characteristics of these (potential) SFRs, we cannot make any firm conclusion. Their spectra are not fully compatible, which can be due to the fact that they are detected at different energies, but also because the emission mechanisms can be different. In the case of 2FHL J1839.5-0705, the uncertainties in the spectral features are due fluctuations/possible contamination introduced by the surrounding sources, and low statistics. We expect to collect more data to increase the statistics and be able to construct an improved SED and obtain more conclusive results.

It is specially interesting the case of the Cygnus Cocoon since it is the only firm case of a SFR observed in VHE (Westerlund 1 and 2, 2FHL J1839.5-0705 and 30 Doradus are still not confirmed as SFRs). *Katsuta et al.* [49] have made a comparison of G25 and Cygnus Cocoon regions, finding a lot of similarities between both sources. These regions have a similar diameter (∼100-200 pc), with OB young and massive associations generating strong stellar winds and super-bubble structures that could potentially be the cause of the particle acceleration in SFRs (more detailed information in Subsection 4.3.7).

We have also estimated the luminosity of 2FHL J1839.5-0705 using Equation (11).

$$L = 4\pi d^2 F \tag{11}$$

F represents the flux of the source and d is the distance to it. Assuming a distance $d \sim$ 7.7 kpc [49], we obtain a luminosity of L=3.69·10^{34} ± 1.45·10^{34} erg s^{-1} at 200 GeV. This value is compatible with the luminosity given by *Katsuta et al.* for the whole region G25 in the range

of 1-100 GeV, L=1.3·10^{36} erg s^{-1}, and comparable to the Cygnus Cocoon luminosity, L=9·10^{34} erg s^{-1}.

4.3.6. Study of Other Sources From Region G25

Since 2FHL J1839.5-0705 lies in a rich active galactic region, we have also tried to extract the spectrum of the three main sources of the region G25, HESS 1837-069, 2FHL J1837.4-0717 and 2FHL 1836.5-0655e. The goal is to properly fit the position of each source via *Caspar* and then use these coordinates to obtain the SED of each source. We have fitted the position of all three sources. For 2FHL J1837.4-0717 and 2FHL 1836.5-0655e, we used the option *Subtractstar* from *Caspar* to eliminate the contribution of HESS J1837-069. However, due to the large extension of HESS J1837-069, which contaminates the γ-ray emission of the nearby sources, the extension fit is not precise, even using this option. This causes that the spectra obtained from these sources are not well estimated. In the case of HESS J1837-069, the emission is too extended to be properly fitted using the standard MAGIC analysis program, MARS. More sophisticated tools are needed in order to eliminate the contribution of HESS J1837-069 and study this region more deeply.

We can obtain though a flux contour skymap, which reflects the relative flux of the sources with contours representing the significance, starting in 5σ, and increasing in steps of 1σ each contour (see Figure 23). Relative flux represents the mean excess events relative to the background density, assuming that this background scales with the effective area. Due to the low significance of 2FHL J1839.5-0705, and the high significance of the nearby source HESS J1837-069, this option could not be used before to identify 2FHL J1839.5-0705.

More advanced tools are needed in order to neglect the contribution of these bright sources and obtain precise results, which could be done in the future with *Skyprism* software, dedicated to extended and off-centered sources, just like our case.

4.3.7. Emission Models

Finally, we will discuss the main acceleration mechanisms proposed to explain the processes taking place in these SFRs. The presence of relativistic particles in these regions suggest that VHE emission appears mainly due to inverse Compton scattering and relativistic Bremsstrahlung processes [50]. There are two main scenarios to explain particle acceleration processes in SFRs.

The first considered mechanism suggests that particle acceleration can take place due to strong stellar winds of massive individual hot stars [50]. The most favored model is triggered by stellar winds, and involves colliding winds from massive binary (or multiple) systems. Electrons and protons can be accelerated in the colliding wind shock, with non-thermal radio emission as indicator of this process. Also, γ-ray emission can happen due to young SFRs and protostars. In the prestellar cores present in these regions, protostellar disks are formed, which can be evidenced through IR observations. Here, magnetic fields are twisted by the infalling matter, creating a magnetic tower. This structure collimates a jet in which particles can be accelerated. The presence of the 2MASS 18392702-0708413 IR source could be indicative that this mechanism is at operation.

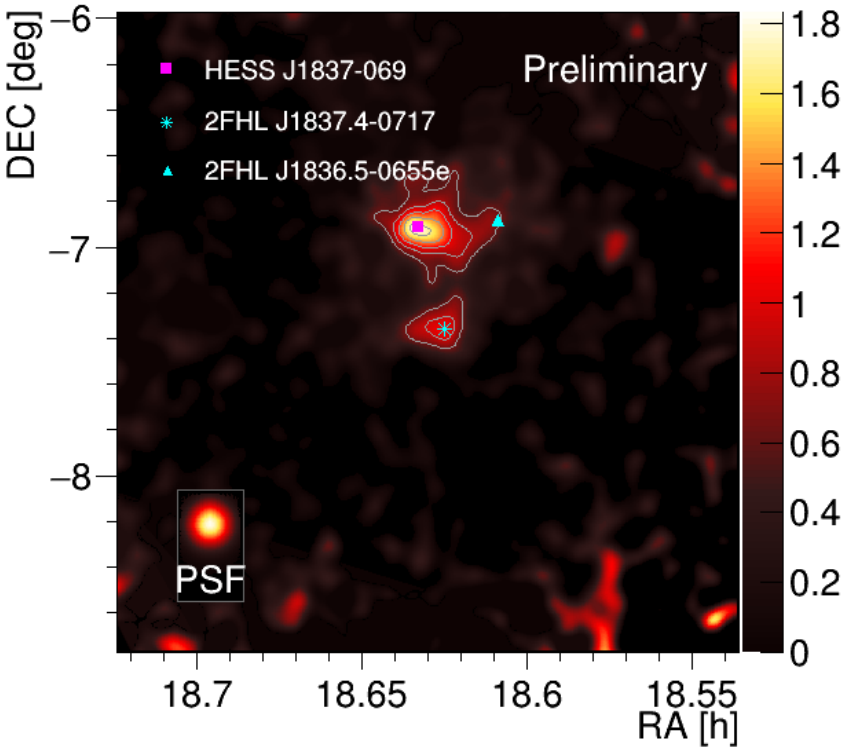

Figure 23: Relative flux contours for HESS J1837-069, 2FHL J1837.4-0717 and 2FHL J1836.5-0655e sources.

In the second scenario, two main models are proposed. The first one assumes that particles trapped inside the bubble are accelerated mainly by magnetic turbulences [49]. In the second model, particles can be accelerated via diffusive shock acceleration (DSA) in which cosmic rays could be produced via diffusion between collisions between interstellar clouds [49]. The theory postulates that photons trying to escape from the bubble and which are powered by stellar winds, interact with the particles in the shock. This interaction increases their energy due to inverse Compton scattering with relativistic electrons [64], producing γ-ray emission. The reason why other HII regions are not detected in VHE could be due to the size difference between super-bubbles like the ones present in region G25 or the Cygnus Cocoon (which are larger by more than one order of magnitude) and the HII regions [65].

These models should be tested in the future once more data is available to understand how photons are accelerated in SFRs and how the proposed mechanisms work. Despite of detecting the source in LE range, which means the first detection of a SFR with the MAGIC telescopes, we are at the edge of detecting the source at E>250 GeV. We expect to be able to test these emission models in further studies when more data is available, so we can increase the statistics.

5. Conclusions

The appearance and development of the IACT technique have opened a new window to observe the Universe and the most violent objects. These improvements led to the detection

of SFRs in VHE, like the Cygnus Cocoon by *Fermi*-LAT. Several candidates to SFRs have appeared since then, like Westerlund 1 and 2 or 2FHL J1839.5-0705.

We have observed 2FHL J1839.5-0705 with the MAGIC telescopes for 30 hours in 2017. We have analyzed data following a non-standard MAGIC analysis due to the extended nature of the source. We have detected the source at LE (>100 Gev, 5.28σ) and FR (>250 GeV, 4.97σ). This could be the second detection of a SFR in the northern hemisphere and the first one with the MAGIC telescopes, in case of confirming its nature. An emission hotspot has been detected at HE (>1 TeV), but this is compatible with statistical fluctuations of the background.

We have studied the lightcurve of the source during three months, to check whether if there is any flux variability over time. The received flux decreases as we go to higher energies, being almost undetectable above 400 GeV. No variability has been observed neither in a daily nor a monthly basis. The source is compatible with a constant flux of $3.25{\cdot}10^{-12} \pm 1.28{\cdot}10^{-12}$ $cm^{-2}s^{-1}$ at 200 GeV.

We have also obtained the spectrum of the source, fitted by a power law of index of α=-3.31 $\pm$ 0.46 and a differential flux normalization at 1 TeV of $f_0=(2.49 \pm 1.78){\cdot}10^{-13}$ $TeV^{-1}cm^{-2}s^{-1}$. All methods used are compatible with each other. The SED, which includes data extracted from *Fermi*-LAT observations and from 2MASS catalog, reveals a posible IR counterpart to 2FHL J1839.5-0705 that could help determining the SFR nature of the source. When comparing with other SFRs (or potential SFRs), we cannot find a clear correlation that reveals the nature of 2FHL J1839.5-0705. It is worth noticing that the low statistics we have in our data have an impact in the fitted parameters of the extracted spectrum and SED.

Other VHE sources are detected in the FoV of 2FHL J1839.5-0705. 2FHL J1837.4-0717 and 2FHL J1836.5-0655e are revealed in the flux contour map as two independent sources from HESS J1837-069 with high significance. However, due to the extension of the sources, the tools used for the analysis and the configuration of the observations, our capabilities to resolve the region are limited.

Different emission models could explain the particle acceleration processes taking place in these regions. These models either assume the presence of a massive OB star/association interacting with a bubble, γ-ray emission triggered by the interaction of stellar winds or interactions in jets of protostellar disks in young SFRs [50]. γ-rays are generated by inverse Compton and Bremsstrahlung processes.

6. Future work

As we have seen in this project, VHE astronomy is one of the most recent fields of study in astrophysics, which implies that there is a lot of future work to improve the current techniques and analysis.

Focusing on the study of 2FHL J1839.5-0705, we had a limited amount of observation time of around 30 hours. It is expected that this year we will have more data from new observations which will help to acumulate more γ-ray events and improve the significance analysis. We will also check archival MAGIC data. Also, with the construction of the first telescope of the Cherenkov Telescope Array (CTA), the Large-Sized Telescope 1 (LST1), with

a diameter of 23 m and a better sensitivity than MAGIC telescopes, data with a higher quality may be available in the future to help understanding this complex region.

Regarding the data analysis, there is still work to do in order to improve the results obtained with the current data. An optimization of the hadronness, energy and size cuts is still pending to be applied to improve the significance. Also, the estimation of the background flux and the normalization in *Odie* analysis can be improved. For this purpose, a new tool can be used in further studies named *Skyprism*, intended for extended and off-centered sources and regions with multiple sources in the FoV [39].

This analysis can be complemented by studying data in other wavelenghts (X-rays, IR, radio) and from other observatories and experiments (*Fermi*-LAT, H.E.S.S.), to study the properties of 2FHL J1839.5-0705 throughout all the electromagnetic spectrum. *Fermi*-LAT data is available and public, and around a 30% of the detected sources do not have a clear association with known objects, so analyzing this unidentified sources can lead to the detection of more SFRs in the range of GeV and TeV.

Finally, the acceleration mechanism in these SFRs is still not clear. Future studies can clarify how γ-rays are accelerated up to GeV and TeV energies in SFRs by testing and cheking the different models proposed, like the one in *Katsuta et al.* [49] or *Gustavo E. Romero* [50], in which a bubble is expected to be created by a massive OB star with stellar winds strong enough to accelerate the particles in this bubble. Studying this and other alternative models can help to comprehend the different processes that take place in these regions.

A. Appendix

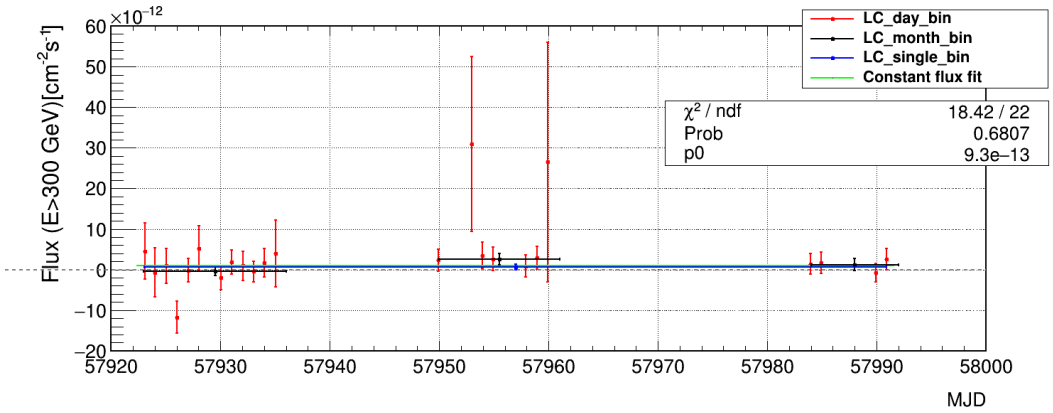

Figure A.1: Lightcurve above 300 GeV. *Red*: Day-by-day integrated flux. *Black*: Monthly integrated flux. *Blue*: Total integrated flux. *Green*: Fitted line for constant integrated flux.

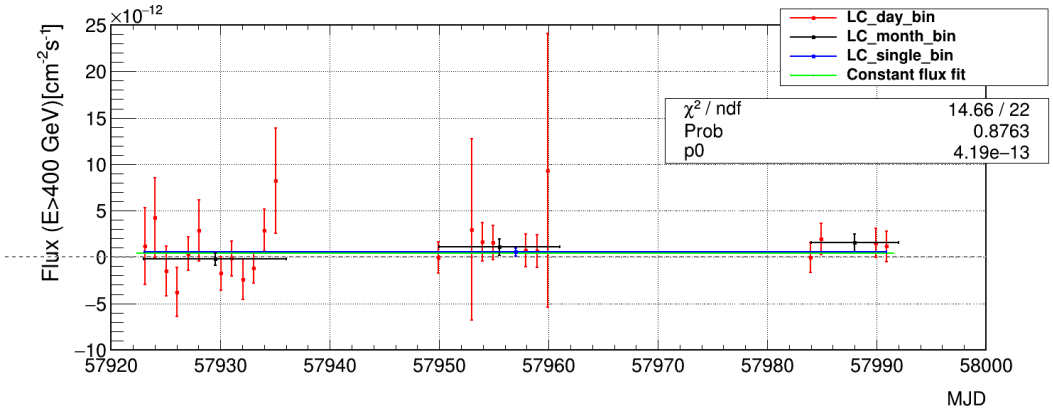

Figure A.2: Lightcurve above 400 GeV. *Red*: Day-by-day integrated flux. *Black*: Monthly integrated flux. *Blue*: Total integrated flux. *Green*: Fitted line for constant integrated flux.

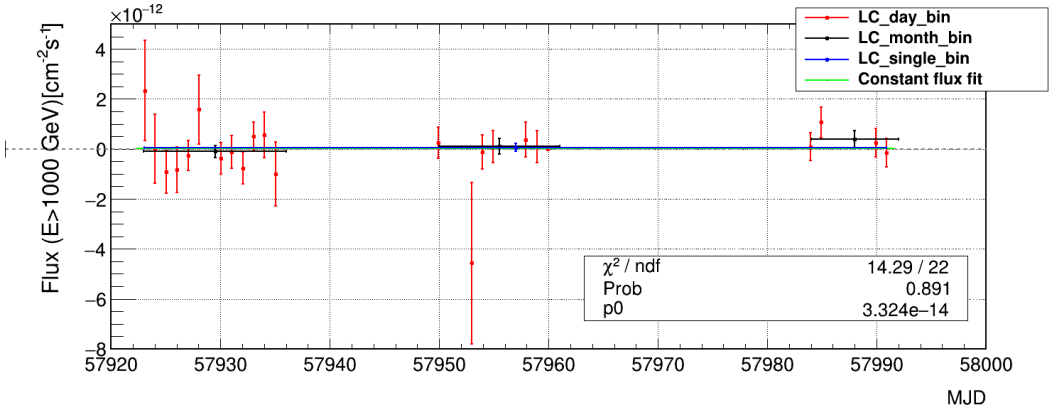

Figure A.3: Lightcurve above 1000 GeV. *Red*: Day-by-day integrated flux. *Black*: Monthly integrated flux. *Blue*: Total integrated flux. *Green*: Fitted line for constant integrated flux.

References

[1] W. Galbraith and J. Jelley, "Light pulses from the night sky associated with cosmic rays," *Nature*, vol. 171, no. 4347, p. 349, 1953.

[2] T. C. Weekes, M. Cawley, D. Fegan, *et al.*, "Observation of TeV gamma rays from the Crab nebula using the atmospheric Cerenkov imaging technique," *The Astrophysical Journal*, vol. 342, pp. 379–395, 1989.

[3] M. Actis, G. Agnetta, F. Aharonian, *et al.*, "Design concepts for the Cherenkov Telescope Array CTA: an advanced facility for ground-based high-energy gamma-ray astronomy," *Experimental Astronomy*, vol. 32, no. 3, pp. 193–316, 2011.

[4] J. Holder, "TeV gamma-ray astronomy: A summary," *Astroparticle Physics*, vol. 39, pp. 61–75, 2012.

[5] Pierre Auger Collaboration and others, "The Pierre Auger cosmic ray observatory," *Nuclear Instruments and Methods in Physics Research Section A: Accelerators, Spectrometers, Detectors and Associated Equipment*, vol. 798, pp. 172–213, 2015.

[6] D. J. Thompson, "Space detectors for gamma rays (100 MeV–100 GeV): From EGRET to Fermi LAT," *Comptes Rendus Physique*, vol. 16, no. 6-7, pp. 600–609, 2015.

[7] S. Funk, "Ground- and Space-Based Gamma-Ray Astronomy," *Annual Review of Nuclear and Particle Science*, vol. 65, pp. 245–277, Oct. 2015.

[8] M. Ackermann, M. Ajello, W. Atwood, L. Baldini, J. Ballet, G. Barbiellini, D. Bastieri, J. B. Gonzalez, R. Bellazzini, E. Bissaldi, *et al.*, "2FHL: the second catalog of hard Fermi-LAT sources," *The Astrophysical Journal Supplement Series*, vol. 222, no. 1, p. 5, 2016.

[9] L. Anchordoqui, T. Paul, S. Reucroft, and J. Swain, "Ultrahigh energy cosmic rays: The state of the art before the Auger observatory," *International Journal of Modern Physics A*, vol. 18, no. 13, pp. 2229–2366, 2003.

[10] Pierre Auger Collaboration, A. Aab, P. Abreu, M. Aglietta, I. A. Samarai, I. F. M. Albuquerque, I. Allekotte, A. Almela, J. Alvarez Castillo, J. Alvarez-Muñiz, and et al., "Observation of a large-scale anisotropy in the arrival directions of cosmic rays above 8 $\times 10^{18}$ eV," *Science*, vol. 357, pp. 1266–1270, Sept. 2017.

[11] A. Abramowski, F. Aharonian, F. A. Benkhali, A. Akhperjanian, E. Angüner, M. Backes, A. Balzer, Y. Becherini, J. B. Tjus, D. Berge, *et al.*, "Acceleration of petaelectronvolt protons in the Galactic Centre," *Nature*, vol. 531, no. 7595, p. 476, 2016.

[12] Cherenkov Telescope Array Consortium, B. S. Acharya, I. Agudo, I. A. Samarai, R. Alfaro, J. Alfaro, C. Alispach, R. Alves Batista, J.-P. Amans, and et al., "Science with the Cherenkov Telescope Array," *ArXiv e-prints*, Sept. 2017.

[13] C. Pfrommer, "Introduction to extragalactic sources of very high-energy photons," *ArXiv e-prints*, Aug. 2013.

[14] B. Abbott, R. Abbott, T. Abbott, F. Acernese, K. Ackley, C. Adams, T. Adams, P. Addesso, R. Adhikari, V. Adya, *et al.*, "Gravitational waves and gamma-rays from a binary neutron star merger: GW170817 and GRB 170817A," *The Astrophysical Journal Letters*, vol. 848, no. 2, p. L13, 2017.

[15] G. Dubus, "Gamma-ray binaries and related systems," *The Astronomy and Astrophysics Review*, vol. 21, no. 1, p. 64, 2013.

[16] F. Aharonian, R. Yang, and E. de Oña Wilhelmi, "Massive Stars as Major Factories of Galactic Cosmic Rays," *ArXiv e-prints*, Apr. 2018.

[17] A. Abramowski, F. Acero, F. Aharonian, A. Akhperjanian, G. Anton, A. Balzer, A. Barnacka, U. B. De Almeida, Y. Becherini, J. Becker, *et al.*, "Discovery of extended vhe γ-ray emission from the vicinity of the young massive stellar cluster Westerlund 1," *Astronomy & Astrophysics*, vol. 537, p. A114, 2012.

[18] M. Lemoine-Goumard, E. Ferrara, M.-H. Grondin, P. Martin, and M. Renaud, "Fermi-LAT detection of gamma-ray emission in the vicinity of the star forming regions W43 and Westerlund 2 ," *Memorie della Societa Astronomica Italiana*, vol. 82, p. 739, 2011.

[19] S. Ohm, D. Horns, O. Reimer, J. Hinton, G. Rowell, E. O. Wilhelmi, M. V. Fernandes, F. Acero, and A. Marcowith, "H.E.S.S. Observations of Massive Stellar Clusters," in *High Energy Phenomena in Massive Stars* (J. Martí, P. L. Luque-Escamilla, and J. A. Combi, eds.), vol. 422 of *Astronomical Society of the Pacific Conference Series*, p. 265, May 2010.

[20] O. Reimer, F. Aharonian, J. Hinton, W. Hofmann, S. Hoppe, M. Raue, and A. Reimer, "VHE gamma-rays from Westerlund 2 and implications for the inferred energetics," in *Clumping in Hot-Star Winds* (W.-R. Hamann, A. Feldmeier, and L. M. Oskinova, eds.), p. 195, Apr. 2008.

[21] A. Abdo, M. Ackermann, M. Ajello, W. Atwood, L. Baldini, J. Ballet, G. Barbiellini, D. Bastieri, B. Baughman, K. Bechtol, *et al.*, "Observations of the large magellanic cloud with Fermi," *Astronomy & Astrophysics*, vol. 512, p. A7, 2010.

[22] T. C. Weekes, *Very high energy gamma-ray astronomy*. CRC Press, 2003.

[23] M. Rao and B. V. Sreekantan, *Extensive air showers*. World scientific, 1998.

[24] J. Matthews, "A Heitler model of extensive air showers," *Astroparticle Physics*, vol. 22, no. 5-6, pp. 387–397, 2005.

[25] P. A. Cherenkov, "Visible emission of clean liquids by action of γ radiation," *Doklady Akademii Nauk SSSR*, vol. 2, p. 451, 1934.

[26] F. A. Aharonian and A. K. Konopelko, "Stereo Imaging of VHE Gamma-Ray Sources," *ArXiv Astrophysics e-prints*, Dec. 1997.

[27] T. C. Weekes, "The Atmospheric Cherenkov Imaging Technique for Very High Energy Gamma-ray Astronomy," *ArXiv Astrophysics e-prints*, Aug. 2005.

[28] A. M. Hillas, "Cerenkov light images of EAS produced by primary gamma," in *International Cosmic Ray Conference*, vol. 3, 1985.

[29] F. Aharonian, A. Akhperjanian, A. Bazer-Bachi, M. Beilicke, W. Benbow, D. Berge, K. Bernlöhr, C. Boisson, O. Bolz, V. Borrel, *et al.*, "Observations of the Crab nebula with HESS," *Astronomy & Astrophysics*, vol. 457, no. 3, pp. 899–915, 2006.

[30] Mazin, D., Tescaro, D., Garczarczyk, M., Giavitto, G. and Sitarek, J. for the MAGIC Collaboration, "Upgrade of the MAGIC telescopes," *ArXiv e-prints*, Oct. 2014.

[31] D. Bastieri, D. Agguiaro, J. Arnold, C. Bigongiari, F. Dazzi, M. Doro, N. Galante, M. Garczarczyk, E. Lorenz, D. Maniero, *et al.*, "The mirrors for the MAGIC telescopes," in *International Cosmic Ray Conference*, vol. 5, p. 283, 2005.

[32] Borla Tridon, D., Goebel, F., Fink, D., Haberer, W., Hose, J., Hsu, C. C., Jogler, T., Mirzoyan, R., Orito, R., Reimann, O., Sawallisch, P., Schlammer, J. and Schweizer, T., Steinke, B. and Teshima, M. for the MAGIC Collaboration, "Performance of the Camera of the MAGIC II Telescope," *ArXiv e-prints*, June 2009.

[33] Tescaro, D., López-Oramas, A., Moralejo, A., Mazin, D. and Daniela Hadasch for the MAGIC Collaboration, "The MAGIC telescopes DAQ software and the on-the-fly online analysis client," *ArXiv e-prints*, Oct. 2013.

[34] Sitarek, J., Carmona, E., Colin, P., Frantzen, K., Gaug, M., Lopez, M., Lombardi, S., Moralejo, A., Satalecka, K., Scapin, V., Stamatescu, V., Zanin, R., Mazin, D. and Tescaro, D. for the MAGIC Collaboration, "Physics performance of the upgraded MAGIC telescopes obtained with Crab Nebula data," *ArXiv e-prints*, Aug. 2013.

[35] M. L. Ahnen, S. Ansoldi, L. Antonelli, P. Antoranz, A. Babic, B. Banerjee, P. Bangale, U. B. De Almeida, J. Barrio, W. Bednarek, *et al.*, "Very High Energy γ-Rays from the Universe's Middle Age: Detection of the z= 0.940 Blazar PKS 1441+25 with MAGIC," *The Astrophysical Journal Letters*, vol. 815, no. 2, p. L23, 2015.

[36] J. Aleksić, S. Ansoldi, L. Antonelli, P. Antoranz, A. Babic, P. Bangale, M. Barceló, J. Barrio, J. B. Gonzalez, W. Bednarek, *et al.*, "The major upgrade of the MAGIC telescopes, Part II: A performance study using observations of the Crab Nebula," *Astroparticle Physics*, vol. 72, pp. 76–94, 2016.

[37] C. Fruck, *A new LIDAR system for the MAGIC telescopes and site search instrumentation for CTA*. PhD thesis, Max Planck Institute for Physics, 2011.

[38] Fruck, C., Gaug, M., Zanin, R., Dorner, D., Garrido, D., Mirzoyan, R. and Font, L. for the MAGIC Collaboration , "A novel LIDAR-based Atmospheric Calibration Method for Improving the Data Analysis of MAGIC," *ArXiv e-prints*, Mar. 2014.

[39] Zanin, R., Carmona, E., Sitarek, J., "MARS, the MAGIC analysis and reconstruction software," in *Proc. of the ICRC 2013 International Cosmic Ray Conference*, 2013.

[40] I. Antcheva, M. Ballintijn, B. Bellenot, M. Biskup, R. Brun, N. Buncic, P. Canal, D. Casadei, O. Couet, V. Fine, *et al.*, "ROOT—A C++ framework for petabyte data storage, statistical analysis and visualization," *Computer Physics Communications*, vol. 182, no. 6, pp. 1384–1385, 2011.

[41] E. Aliu, H. Anderhub, L. Antonelli, P. Antoranz, M. Backes, C. Baixeras, J. Barrio, H. Bartko, D. Bastieri, J. Becker, *et al.*, "Improving the performance of the single-dish Cherenkov telescope MAGIC through the use of signal timing," *Astroparticle Physics*, vol. 30, no. 6, pp. 293–305, 2009.

[42] J. Aleksić, E. Alvarez, L. Antonelli, P. Antoranz, M. Asensio, M. Backes, J. Barrio, D. Bastieri, J. B. González, W. Bednarek, *et al.*, "Performance of the MAGIC stereo system obtained with Crab Nebula data," *Astroparticle Physics*, vol. 35, no. 7, pp. 435–448, 2012.

[43] M. Will, "Atmospheric Monitoring at the Site of the MAGIC Telescopes," in *EPJ Web of Conferences*, vol. 144, p. 01002, EDP Sciences, 2017.

[44] A. López Oramas, *Multi-year campaign of the gamma-ray binary LS I+61º 303 and search for VHE emission from gamma-ray binary candidates with the MAGIC telescopes.* PhD thesis, 2014.

[45] T.-P. Li and Y.-Q. Ma, "Analysis methods for results in gamma-ray astronomy," *The Astrophysical Journal*, vol. 272, pp. 317–324, 1983.

[46] J. Albert, E. Aliu, H. Anderhub, P. Antoranz, A. Armada, M. Asensio, C. Baixeras, J. Barrio, H. Bartko, D. Bastieri, *et al.*, "Unfolding of differential energy spectra in the MAGIC experiment," *Nuclear Instruments and Methods in Physics Research Section A: Accelerators, Spectrometers, Detectors and Associated Equipment*, vol. 583, no. 2-3, pp. 494–506, 2007.

[47] G. Gumiero, "Analysis of the Two Gamma-Ray Flares of the BL-Lac RGB 0521+212 observed by MAGIC," 2014.

[48] N. Murray and M. Rahman, "Star formation in massive clusters via the Wilkinson Microwave Anisotropy Probe and the Spitzer Glimpse survey," *The Astrophysical Journal*, vol. 709, no. 1, p. 424, 2009.

[49] J. Katsuta, Y. Uchiyama, and S. Funk, "Extended gamma-ray emission from the G25.0+0.0 region: A star-forming region powered by the newly found OB association?," *The Astrophysical Journal*, vol. 839, no. 2, p. 129, 2017.

[50] G. E. Romero, "Gamma rays from star-forming regions," in *AIP Conference Proceedings*, vol. 1085, pp. 97–103, AIP, 2008.

[51] H. Abdalla, A. Abramowski, F. Aharonian, F. A. Benkhali, E. Angüner, M. Arakawa, M. Arrieta, P. Aubert, M. Backes, A. Balzer, *et al.*, "The HESS Galactic plane survey," *Astronomy & Astrophysics*, vol. 612, p. A1, 2018.

[52] J. Lande, M. Ackermann, A. Allafort, J. Ballet, K. Bechtol, T. H. Burnett, J. Cohen-Tanugi, A. Drlica-Wagner, S. Funk, F. Giordano, M.-H. Grondin, M. Kerr, and M. Lemoine-Goumard, "Search for Spatially Extended Fermi Large Area Telescope Sources Using Two Years of Data," *Astrophysical Journal*, vol. 756, p. 5, Sept. 2012.

[53] E. Gotthelf and J. Halpern, "Discovery of a Young, Energetic 70.5 ms Pulsar Associated with the TeV Gamma-Ray Source HESS J1837–069," *The Astrophysical Journal*, vol. 681, no. 1, p. 515, 2008.

[54] A. Abeysekara, A. Albert, R. Alfaro, C. Alvarez, J. Álvarez, R. Arceo, J. Arteaga-Velázquez, H. A. Solares, A. Barber, B. Baughman, *et al.*, "The 2HWC HAWC observatory gamma-ray catalog," *The Astrophysical Journal*, vol. 843, no. 1, p. 40, 2017.

[55] A. Abeysekara, R. Alfaro, C. Alvarez, J. Álvarez, R. Arceo, J. Arteaga-Velázquez, H. A. Solares, A. Barber, B. Baughman, N. Bautista-Elivar, *et al.*, "Search for TeV Gamma-Ray Emission from Point-like Sources in the Inner Galactic Plane with a Partial Configuration of the HAWC Observatory," *The Astrophysical Journal*, vol. 817, no. 1, p. 3, 2016.

[56] G. Ferrand and S. Safi-Harb, "A census of high-energy observations of Galactic supernova remnants," *Advances in Space Research*, vol. 49, no. 9, pp. 1313–1319, 2012.

[57] G. Ferrand and S. Safi-Harb, "Galactic Supernova Remnants Catalog: `http://www.physics.umanitoba.ca/snr/SNRcat/`," accesed at 04/2018.

[58] M. Ackermann, M. Ajello, L. Baldini, J. Ballet, G. Barbiellini, D. Bastieri, R. Bellazzini, E. Bissaldi, E. Bloom, R. Bonino, *et al.*, "Search for Extended Sources in the Galactic Plane Using Six Years of Fermi-Large Area Telescope Pass 8 Data above 10 GeV," *The Astrophysical Journal*, vol. 843, no. 2, p. 139, 2017.

[59] M. Skrutskie, R. Cutri, R. Stiening, M. Weinberg, S. Schneider, J. Carpenter, C. Beichman, R. Capps, T. Chester, J. Elias, *et al.*, "The two micron all sky survey (2MASS)," *The Astronomical Journal*, vol. 131, no. 2, p. 1163, 2006.

[60] M. Rahman and N. Murray, "A New Sample of Very Massive Star Forming Complexes in the Spitzer Glimpse Survey," *Astrophysical Journal*, vol. 719, pp. 1104–1122, Aug. 2010.

[61] T. R. Geballe, "Infrared spectroscopy of star-forming regions - Some recent results of interest," *Publications of the ASP*, vol. 95, pp. 556–564, Sept. 1983.

[62] J. M. Jackson, R. Simon, R. Shah, J. Rathborne, M. H. Heyer, D. P. Clemens, and T. M. Bania, "The Boston University-FCRAO Galactic Ring Survey," in *Milky Way Surveys: The Structure and Evolution of our Galaxy* (D. Clemens, R. Shah, and T. Brainerd, eds.), vol. 317 of *Astronomical Society of the Pacific Conference Series*, p. 49, Dec. 2004.

[63] B. Bartoli, P. Bernardini, X. Bi, P. Branchini, A. Budano, P. Camarri, Z. Cao, R. Cardarelli, S. Catalanotti, S. Chen, *et al.*, "Identification of the TeV gamma-ray source ARGO J2031+ 4157 with the Cygnus Cocoon," *The Astrophysical Journal*, vol. 790, no. 2, p. 152, 2014.

[64] M. G. Baring, "Diffusive Shock Acceleration : the Fermi Mechanism.," in *Very High Energy Phenomena in the Universe; Moriond Workshop* (Y. Giraud-Heraud and J. Tran Thanh van, eds.), p. 97, 1997.

[65] G. Maurin, A. Marcowith, N. Komin, F. Krayzel, and G. Lamanna, "Embedded star clusters as sources of high-energy cosmic rays . Modelling and constraints," *Astronomy & Astrophysics*, vol. 591, p. A71, June 2016.

[66] A. A. Abdo, M. Ackermann, M. Ajello, A. Allafort, E. Antolini, W. B. Atwood, M. Axelsson, L. Baldini, J. Ballet, G. Barbiellini, and et al., "Fermi Large Area Telescope First Source Catalog," *Astrophysical Journal, Supplement*, vol. 188, pp. 405–436, June 2010.